

Scaled biomass estimation in woodland ecosystems: Testing the individual and combined capacities of satellite multispectral and lidar data

Michael J. Campbell ^{a,*}, Philip E. Dennison ^a, Kelly L. Kerr ^b, Simon C. Brewer ^a, William R. L. Anderegg ^b

^a Department of Geography, University of Utah, Salt Lake City, UT 84112, United States of America

^b School of Biological Sciences, University of Utah, Salt Lake City, UT 84112, United States of America



ARTICLE INFO

Edited by: Jing M. Chen

Keywords:

Aboveground biomass
Woodland ecosystems
Airborne lidar
Landsat
GEDI
Scaled modeling

ABSTRACT

Airborne laser scanning (ALS) data enable accurate modeling and mapping of aboveground biomass (AGB), but the limited spatial and temporal extents of ALS data collection limit the capacity for broad-scale carbon accounting. Conversely, while space-based remote sensing instruments provide increased spatial and temporal coverage, it can be difficult to directly link field-level vegetation biometrics to satellite data due to coarser spatial resolution and positional uncertainty. The combined use of ALS and satellite remote sensing data may offer a solution to efficient, accurate, and consistent AGB mapping across time and space. Such airborne-spaceborne data fusion has been demonstrated successfully in high-biomass settings; however, the unique structural conditions of dryland woodland ecosystems, with open canopies and low leaf area indices, pose mapping challenges that require further study. These challenges are particularly acute with large footprint spaceborne lidar, where short, widely-spaced trees may limit the capacity for accurate AGB estimation. In this study, we present a scaled methodological framework for linking field-measured woodland AGB to ALS data and, in turn, linking ALS-modeled AGB to satellite data, using piñon-juniper woodlands in southeastern Utah as a case study. We compare the effectiveness of this scaling approach using two satellite sensors, Landsat 8 OLI (multispectral) and GEDI (lidar). Since the predicted outputs of our local-scale model are being used as inputs to our regional-scale model, we also demonstrate an approach for propagating uncertainty throughout this nested, multiscale analytical framework, leveraging the inherent variability within a random forest's decision trees. Given the positional uncertainty of GEDI footprints, we test a range of different footprint sizes for their relative effects on ALS-GEDI AGB model accuracy. Our local-scale (field-ALS) predictive model was able to account for 74% of variance in AGB, and estimate AGB with a root mean squared error (RMSE) of 14 Mg/ha, a mean absolute error (MAE) of 11.09 Mg/ha. Our regional-scale (ALS-Landsat/GEDI) analysis with propagated uncertainty revealed that the combined use of Landsat and GEDI metrics produced the best predictive model ($R^2 = 0.68$; RMSE = 12.71 Mg/ha; MAE = 9.40 Mg/ha), followed by Landsat-only metrics ($R^2 = 0.66$, RMSE = 13.08 Mg/ha; MAE = 9.71 Mg/ha), and GEDI-only metrics ($R^2 = 0.49$, RMSE = 16.01 Mg/ha; MAE = 12.14 Mg/ha). These results suggest that Landsat may be better-suited than GEDI for estimating AGB in woodland environments where low canopy covers and short trees limit the capacity for precisely characterizing vegetation structure within large-footprint, waveform lidar data. The footprint size analysis revealed that larger simulated footprints (e.g., 30 m radius and greater) produced higher GEDI model accuracies; however, increasing footprint radii beyond 30 m does not significantly increase model accuracy. This research represents an important step forward in improving our capacity for reliably mapping woodland AGB, and provides an early test case for the application of GEDI data to woodland AGB mapping.

1. Introduction

To better understand the role that vegetation plays in the global

carbon cycle requires accurate, spatially-explicit, and temporally-consistent estimates of aboveground biomass (AGB) (Goetz and Dubayah, 2011). AGB is a readily-measurable proxy for the amount of

* Corresponding author.

E-mail address: mickey.campbell@geog.utah.edu (M.J. Campbell).

carbon stored in a plant, giving it unique importance in the estimation of current carbon stocks (Brown, 2002). In this capacity, it also allows for the measurement of carbon fluxes, including net losses over time due to natural or anthropogenic vegetation removal, and net gains due to growth, recruitment, and expansion (Gibbs et al., 2007). As with most vegetation biometrics, the most accurate way to quantify AGB is using field-based measures. This is typically done through destructive sampling and the development of statistically-based allometric relationships between physical plant dimensions and AGB (Chojnacky et al., 2014). While these allometric relationships are valuable, this analytical approach is practically limited and does not allow for broad-scale AGB estimation (Lu, 2006). Remote sensing techniques uniquely have capacity for providing accurate, objective estimates of AGB on broad spatial and temporal scales (Hudak et al., 2012).

The most accurate, remote sensing-based approach for estimating AGB is through the use of light detection and ranging (lidar) technology (Zolkos et al., 2013). Individual pulses of light are emitted in rapid succession from an airborne platform towards the ground surface, exploiting small gaps in a canopy to capture measurements of three-dimensional vegetation structure (Lefsky et al., 2002). Critical predictors of AGB such as vegetation height and canopy cover can be easily derived from an airborne laser scanner (ALS) point cloud (e.g., Hollaus et al., 2006; Korhonen et al., 2011). The most common approach to mapping AGB using ALS is through the area-based approach (Næsset, 2002), whereby ground reference data are collected within a fixed-area plot, which are fed through species-specific allometric equations to produce a plot-level AGB estimate, which is then compared to a suite of point cloud metrics, using a regression or machine learning algorithm (e.g., Kankare et al., 2013; Luo et al., 2019). Although the effectiveness of this approach has been widely demonstrated, it has some critical limitations: (1) the high cost of data collection and the voluminous nature of ALS point cloud data result in limited spatial extents of data availability; (2) the airborne, opportunistic nature of data collection result in limited temporal data availability; and (3) the range of different sensor specifications and collection parameters limit the transferability of ALS-AGB algorithms derived in one location to another.

One way to overcome these limitations is through the use of more spatially exhaustive, temporally repetitive, and consistently-calibrated satellite data. A wide range of passive remote sensing instruments measuring reflected solar radiance have been explored for their AGB estimation capacity, including coarse spatial resolution sensors like MODIS (e.g., Li et al., 2018), moderate resolution sensors like Landsat 8 OLI and Sentinel-2 (e.g., Askar et al., 2018; Nguyen et al., 2020), and high resolution sensors like Worldview (e.g., Vastaranta et al., 2018). Although these multispectral sensors tend to enable a more broad-scale analysis, they lack the capacity for measuring vegetation structure directly and suffer from spectral saturation in densely-vegetated environments, limiting their ability to directly map AGB (Pflugmacher et al., 2014). The use of space-based lidar instruments, such as the Geoscience Laser Altimeter System (GLAS) onboard the IceSAT and IceSat-2 satellites, as well as the Global Ecosystem Dynamics Investigation (GEDI) onboard the International Space Station may bridge the gap between ALS data and spaceborne passive instruments, providing new and fertile ground for consistent, reliable AGB estimation on a global or near-global scale (Dubayah et al., 2020; Duncanson et al., 2020). Although space-based lidar has demonstrated promise in AGB mapping, through analysis of real and simulated data (Narine et al., 2019; Qi et al., 2019), the point-based data collection approach inherent to these missions does not enable the provision of a spatially-exhaustive AGB estimate. This limits the ability to, for example, derive total AGB estimates for a given location, or vegetation type.

Individually, all of the aforementioned approaches (ground-level, ALS, passive satellite, and active satellite) to mapping AGB are inherently limited. However, by combining these different datasets together, we can leverage their individual strengths and overcome their weaknesses to produce the best possible, spatially- and temporally-explicit

AGB estimates. Data fusion approaches have gained much attention in the remote sensing literature in recent years (Schmitt and Zhu, 2016; Zhang, 2010). One of the most common approaches to data fusion is to link datasets collected at different scales and resolutions. High spatial resolution, local-scale ALS and coarser spatial resolution, regional-scale multispectral satellite data have been fused for scaling estimates of tree mortality (Campbell et al., 2020), canopy height (Hudak et al., 2002), and land cover (Singh et al., 2012). In addition, a small number of studies have linked local-scale ALS data to multispectral satellite imagery to enable regional-scale AGB estimation (Asner et al., 2018; Lu et al., 2012; Luther et al., 2019; Xu et al., 2017; Zald et al., 2016). With respect to active sensor satellite data, it has been suggested that ALS should act as an intermediary between field and space-acquired waveforms for calibrating AGB models in order to minimize prediction error due to geolocation uncertainty (Duncanson et al., 2019). Success in ALS-active satellite scaled AGB modeling has been demonstrated with GLAS (Popescu et al., 2011), but given the nascent of GEDI, we have yet to fully explore its potential and limitations. Thus, it is important to test the extent to which local-scale ALS data can be used in a scaled modeling context to enable regional-scale AGB estimation using spaceborne lidar data from GEDI.

In addition to the inherent strengths and weaknesses of different remote sensing platforms and sensors, the ability to accurately map AGB is also affected by the ecosystem being studied. Research into remote sensing of AGB has revolved heavily around high-biomass forests in humid tropic and subtropical environments, given their relatively large contribution to the global carbon budget (e.g., Clark et al., 2011; Drake et al., 2002; Dubayah et al., 2010; Foody et al., 2003). Indeed, both Asner et al. (2018) and Xu et al. (2017) have successfully demonstrated ALS-satellite multispectral AGB scaled modeling in tropical environments. Likewise, there are a large number of studies inquiring into the capacity for remote sensing to estimate biomass in high-biomass boreal forests (e.g., Dong et al., 2003; Matasci et al., 2018; Muukkonen and Heiskanen, 2005; Næsset and Gobakken, 2008; Rauste, 2005). Scaled AGB modeling has been shown to be effective in these higher-latitude ecosystems (Luther et al., 2019; Zald et al., 2016). However, considerably less attention in the scientific literature has been paid towards lower-biomass dryland woodland ecosystems. Woodland ecosystems possess low-to-moderate tree cover, existing on a spectrum between higher-cover forest ecosystems and lower-cover savanna ecosystems (Ratnam et al., 2011; Taft, 1997). Open-canopy dryland woodland ecosystems are found on approximately 550 Mha globally, representing 4% of all terrestrial land, and spanning every continent besides Antarctica (Bastin et al., 2017). Despite their lower overall biomass, the dynamism of these semiarid ecosystems positions them as a major contributor to interannual variability in the global land carbon sink (Ahlström et al., 2015; Poulter et al., 2014). They exist at a critical environmental threshold, receiving just enough moisture to support the existence of trees. This gives small differences in precipitation a large influence on biomass, as droughts can induce widespread tree mortality (biomass reduction) and moist periods can bring about significant afforestation (biomass increase) (Clifford et al., 2013; Mitchard and Flintrop, 2013).

Remote sensing in semiarid and arid ecosystems poses significant challenges not faced in other, more mesic environments (Krofcheck et al., 2014; Okin et al., 2001; Smith et al., 2019). Trees tend to be short in stature and feature irregularly-shaped crowns (Campbell et al., 2020). Open canopies and relatively low leaf area indices result in an abundance of understory shrubs, grasses, and forbs, as well as bare soil and rock when viewed from the synoptic remote sensing perspective (Smith et al., 2019). While a small number of studies have demonstrated successful AGB mapping in dryland woodland ecosystems using ALS (e.g., Krofcheck et al., 2016), relatively few studies to date have attempted to scale local, ALS-driven woodland AGB estimates to the regional scale using satellite data. Given the vegetation structural differences between tropical and boreal environments, both of which have been well-studied

with respect to scaled ALS-satellite scaled AGB mapping (Asner et al., 2018; Luther et al., 2019; Xu et al., 2017; Zald et al., 2016), and dryland environments, which have not, there is a critical need to understand the best practices for developing broad-scale estimates of open-canopy woodland AGB. Additionally, the vast majority of AGB scaling studies that exist rely on passive optical remote sensing data (e.g., Landsat) as the basis of regional-scale mapping. Particularly given the recent launch of GEDI, there is an additional need to understand the relative strengths and limitations of passive multispectral and active lidar data in scaled AGB modeling.

In this study, we: (1) use ALS data to map AGB on a local scale in an open-canopy woodland environment; (2) use those estimates to map AGB on a regional scale using Landsat imagery and GEDI waveforms, comparing their individual and combined model accuracies; (3) determine which multispectral and waveform predictor variables are most closely-associated with woodland AGB; and (4) compare the effects of different scaled footprint sizes on model accuracy; (5) examine the extent to which adding ancillary climate and topography variables improves AGB predictions; (6) demonstrate a repeatable approach for computing the propagated uncertainty that results from using local-scale modeled estimates to drive a regional-scale predictive model; (7) test the effects of spatial autocorrelation on regional scale model performance.

2. Methods

2.1. Study area

This study is based in the original extent of Bears Ears National Monument (BENM) in southeastern Utah, USA (Fig. 1). BENM was established by presidential proclamation in 2016 as a nearly 6000 km² protected area that possesses immense cultural, historic, and ecological importance. Approximately one year later, it was dramatically reduced in size by a second presidential proclamation (Creadon and Bergren, 2019). However, there is currently a movement underway to restore the monument to its original extent (Nordhaus, 2021). This gives unique

and timely importance to understanding the implications of protecting the cultural and natural resources of BENM, including its abundance of woodland vegetation. We selected the original extent of BENM as our study area because of this woodland dominance and because ALS data were captured within a portion of the Monument in 2018, enabling us to quantify the amount and distribution of woodland AGB within this important setting. The dominant woodland type within BENM is piñon-juniper (PJ). Although PJ woodlands encompass a wide variety of codominant species of piñon pines and junipers, in this study area, the two most common species are twoneedle piñon (*Pinus edulis*) and Utah juniper (*Juniperus osteosperma*). PJ woodlands tend to be low in canopy cover, averaging 16.2% cover within the ALS data extent (Fig. 1C), with trees short in stature (mean = 5.5 m) (LANDFIRE, 2020). As discussed in the Introduction, these structural conditions create unique challenges for remote sensing in PJ woodlands (Campbell et al., 2020).

2.2. ALS data

ALS data were collected in five PJ-dominant areas in the study area on June 2nd, 2018 (Fig. 1C). The areas were specifically designed to capture a wide range of PJ AGB, along an environmental gradient from lower, warmer, drier areas that tend to possess lower AGB to higher, cooler, moister areas that tend to possess higher AGB. A comparison between the distributions of elevation, annual average temperatures and precipitation totals of the ALS data collection areas and BENM can be seen in Fig. 2. The five areas encompass 231.2 km² in total, ranging in elevation from 1654 m at the low end to 2762 m at the high end. The data were captured using an Optech Titan sensor, which emits laser pulses in three distinct wavelengths: green (532 nm), near infrared (1064 nm), and shortwave infrared (1550 nm). Multispectral ALS data such as these have gained attention in the scientific literature in recent years due to increased availability (e.g., Hopkinson et al., 2016; Wallace et al., 2012), but to our knowledge, have not been applied in the context of AGB mapping. Given their capacity for not only mapping three-dimensional structure but also potentially providing valuable

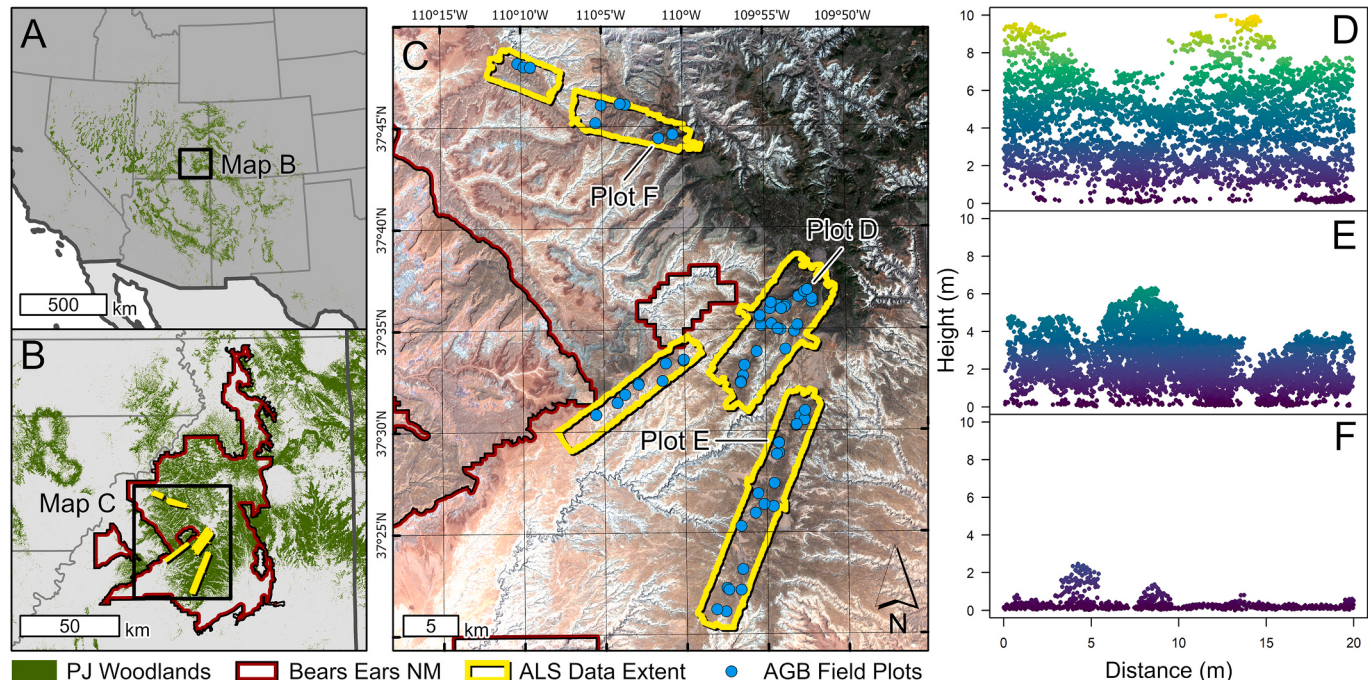


Fig. 1. Study area map with three scales depicted: (A) southwestern United States; (B) the original 2016 extent of Bears Ears National Monument in southeastern Utah with ALS data extent highlighted in yellow; and (C) ALS data extent with field plot locations. Also included are three 20 × 20 m ALS data subsets within field plot areas representing high (D), moderate (E), and low (F) biomass conditions. PJ woodlands extent derived from LANDFIRE Existing Vegetation Type data (LANDFIRE, 2020). (For interpretation of the references to color in this figure legend, the reader is referred to the web version of this article.)

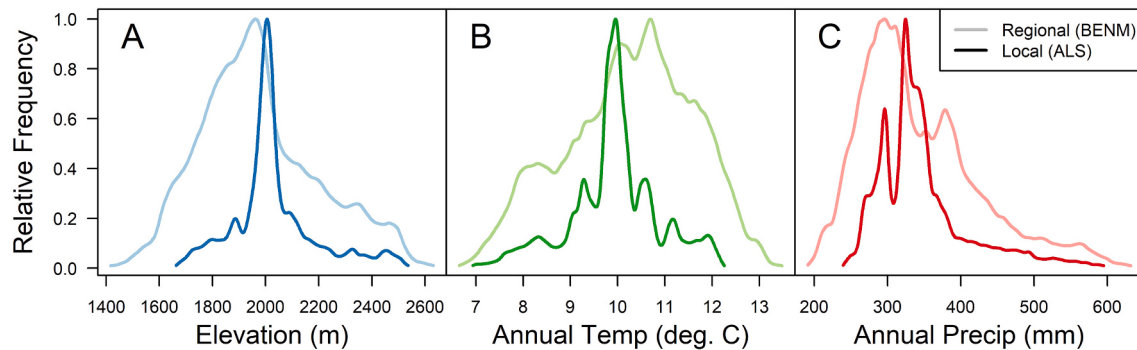


Fig. 2. Relative abundance, as depicted by normalized kernel density distributions, of elevation (A), annual average temperatures (B), and annual precipitation totals (C) between the local-scale ALS data collection areas and the regional-scale BENM. Climate data derived from PRISM (PRISM Climate Group, Oregon State University, 2019).

multiplespectral intensity data for distinguishing between different surface types, it is conceivable that multiplespectral ALS data could improve AGB model predictive power. With a nominal flying height of 600 m, a pulse frequency of 125 kHz, and a scan angle range of $\pm 23^\circ$, the resulting point cloud, merged between the three spectral bands, featured an average pulse density of 21.4 pulses/m².

2.3. Analysis overview

An overview of our analytical approach can be seen in Fig. 3. For the purpose of this study, we will define three analytical scales. The first scale, henceforth “plot scale”, takes place at the scale of the individual field plot. This is the scale at which field data were collected and AGB estimates derived through tree diameter-based allometry (described in

Section 2.4). Taken together, these plots are distributed throughout the extent of our ALS data collection, which we refer to as “local scale”. We first model AGB at the local scale by comparing field-measured AGB to spatially-coincident ALS structural metrics (described in Section 2.5). While it is useful to understand the spatial distribution of PJ AGB across the five collection areas shown in Fig. 1C, our ultimate goal is to map AGB throughout the entirety of BENM (Fig. 1B). To estimate AGB at the scale of BENM, henceforth known as the “regional scale”, we take the results the local-scale AGB modeling process and use those as reference data for generating a regional-scale model (described in Section 2.6). The regional-scale model is driven by spaceborne remotely-sensed data, along with ancillary spatial datasets representing climatic and topographic conditions, that are not as limited in spatial extent as the ALS data. Data preparation, analysis, and modeling for this study took place

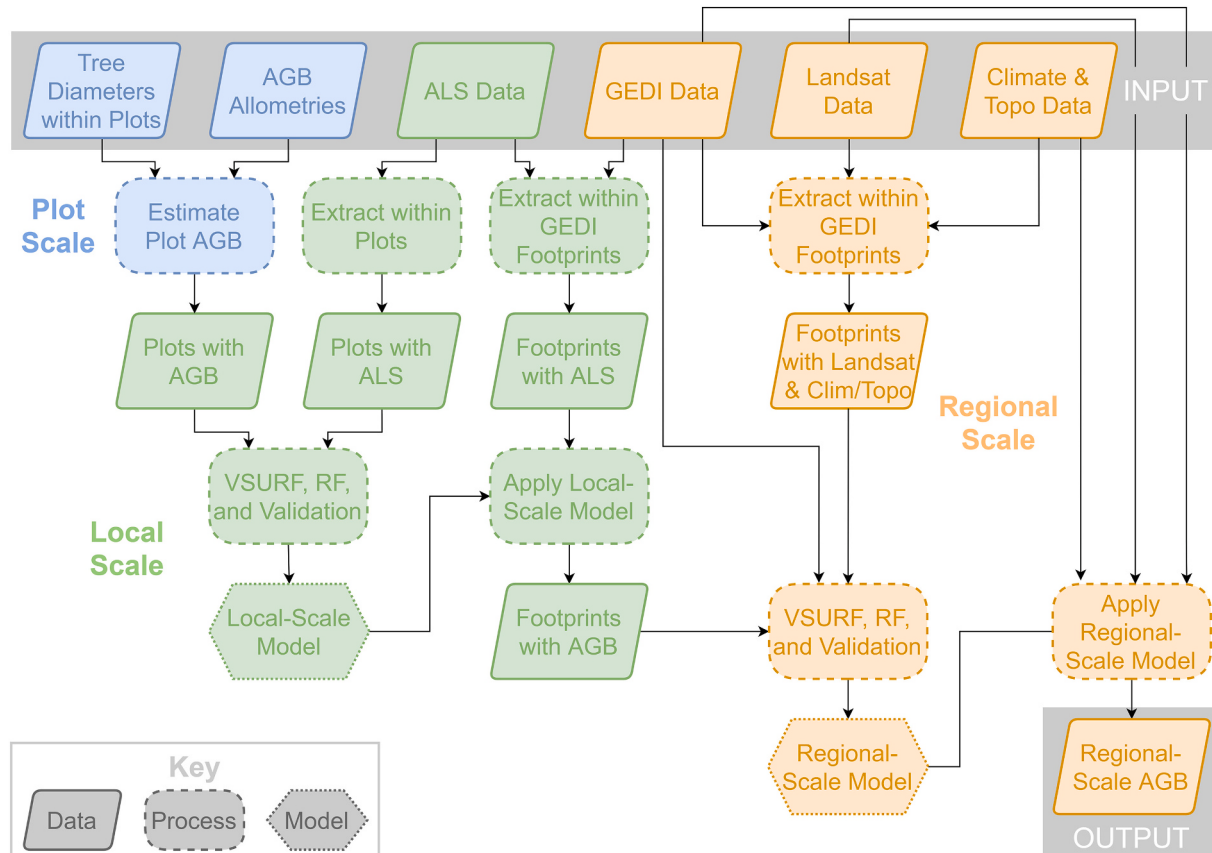


Fig. 3. Overview of the scaled analysis approach used in this study, including the three nominal analytical scales.

using a combination of Esri ArcGIS Pro, Python, and R (R Core Team, 2018), with functions from the following R libraries: lidR (Roussel et al., 2020), randomForest (Cutler and Wiener, 2018), raster (Hijmans and van Etten, 2014), rfUtilities (Evans and Murphy, 2019), rgdal (Bivand et al., 2021), rGEDI (Silva et al., 2020), rgeos (Bivand et al., 2020), VSURF (Genuer et al., 2015), and their various dependencies.

In addition to testing the abilities of spaceborne remote sensing data to model regional-scale AGB, we also examine the extent to which adding ancillary climate and topography data to the modeling process affects model performance (described in Section 2.7). Because the reference data that are driving the regional-scale model are themselves a modeled product and, as a result, possess inherent uncertainty, error must be propagated through the entire modeling process in order to understand regional model performance. Our process for propagating uncertainty is described in Section 2.8. Lastly, the reference data being used for the regional-scale analysis are defined by the positions of GEDI footprints. Because GEDI footprints can be as close as 60 m from one another, it is important to account for the potential effects of spatial autocorrelation on model performance. To account for these effects, we perform a buffered leave-one-out cross-validation (BLOOCV) procedure, described in Section 2.9.

2.4. Field data and biomass allometry

Field data were collected within 65 circular plots within the ALS data extent between 2018 and 2020 (Fig. 1C; Table S2). The plots were circular, with 59 plots having 15 m radii and 6 plots having 18 m radii. Plot locations were guided by a stratification process aimed at capturing a wide range of terrain and climatic variability. Plot centers were navigated to and recorded with a Trimble Geo7x GPS unit, the post-processing of which resulted in average positional error of ± 0.36 m. Plot radii were measured using a TruPulse 360 laser rangefinder. Within each plot, all standing live and dead trees with diameters larger than 4 cm were counted and measured. Diameters were either recorded either at breast height (DBH) or at the root collar (DRC). Since most allometric equations for piñon and juniper trees rely on DRC measurements, all DBH were converted to DRC, using the DRC-DBH allometries defined by Chojnacky and Rogers (1999). Juniper trees in this region can frequently take a multi-stemmed form. When these were encountered in the field, multiple stems were measured and a single DRC was derived using the root-sum-square formula defined in the USDA Forest Service Forest Inventory and Analysis protocol (Bechtold and Patterson, 2005). These DRC measurements (in cm) were used in conjunction with the DRC-AGB allometries defined by Grier et al. (1992). Numerous piñon and juniper allometries exist (e.g., Chojnacky et al., 2014; Cunliffe et al., 2020; Miller et al., 1981; Sprinkle and Klepac, 2015), but those of Grier et al. were chosen due to a combination of both geographic and ecological similarity to our study area and the production of relatively conservative AGB estimates in comparison to others. In addition to diameters, the condition of each tree was recorded as a proportion of live canopy. Per-plot live AGB was calculated as the sum of each individual tree's proportional live AGB. It is important to note that only trees were considered in the calculation of total AGB in this study. AGB from grasses, forbs, shrubs, litter, and debris – all of which are quite minor in this system – were not considered.

2.5. Local-scale AGB modeling (Field – ALS)

The next major step in our scaled modeling procedure involved comparing field data to ALS data. To do this, plot center points were buffered by their respective radii (either 15 or 18 m), and used to clip out individual plot-level subsets of ALS point cloud data. Within each of these point cloud subsets, we first derived a series of topographic variables using the points classified as “ground” returns by the vendor, including elevation, slope, cosine transformation of aspect, sine transformation of aspect, topographic position index (TPI), terrain

ruggedness index (TRI), and ground surface roughness (Hijmans and van Etten, 2014; Wilson et al., 2007). In addition, a series of aboveground point cloud metrics were derived using ground height-normalized data (Table 1). All ALS data processing was performed in R using the lidR library, with additional raster and vector data processing provided by the raster, rgdal, and rgeos libraries (Bivand et al., 2021, 2020; Hijmans and van Etten, 2014; R Core Team, 2018; Roussel et al., 2020).

Terrain, structural, and intensity metrics were combined and compared to plot-level AGB estimates. However, given the large number of predictor variables ($n = 131$), and the comparably small number of plots ($n = 65$), we had to first perform a variable selection procedure. To do this, we employed the use of the variable selection using random forest (VSURF) algorithm of Genuer et al. (2015). This algorithm uses a three-staged procedure that iteratively uses random forests to remove variables that bear little relationship to the outcome variable (step 1), variables that are not needed for accurate prediction (step 2), and finally variables that are redundant (step 3). The resulting, parsimonious set of predictor variables was then used to create a random forest model for predicting AGB as a function of some combination of ALS structural and intensity metrics using the randomForest library in R (Breiman, 2001; Cutler and Wiener, 2018). To evaluate model performance, we used a cross validation procedure implemented in the rfUtilities library by Evans and Murphy (2019). This approach performs a bootstrapping analysis, with 99 iterations, whereby 10% of the samples are randomly selected and withheld for cross-validation on each iteration and compared to a random forest model generated using the other 90% of data. Variable importance was evaluated for the final model as a percent increase in mean square prediction error that would result when a given variable is removed from consideration. Models were evaluated according to the proportion of variance explained (R^2 ; Eq. 1), the root mean square error (RMSE; Eq. 2), the mean absolute error (MAE; Eq. 3), and bias (Eq. 4), as follows:

Table 1

Plot-level ALS structural metrics generated from ground height-normalized point cloud data used as predictor variables for local-scale AGB modeling. With the exception of canopy cover (cc), which was derived from first returns only, metrics were derived using all point returns. For a detailed description of the distinction between vertical relative point density (vrd.x.y) and vertical normalized relative point density (vnrd.x.y), please refer to Campbell et al. (2018).

Abbreviation	Metric
cc	Canopy cover: number of first returns at or above breast height (1.37 m) divided by total number of first returns
cd	Canopy density: number of all returns at or above breast height (1.37 m) divided by total number of all returns
p.x	x th height percentile of rank-ordered point heights from 5th to 100th at a 5 percentile interval
mh	Mean of all point heights
mh.ag	Mean of aboveground point heights
sd	Standard deviation of all point heights
sd.ag	Standard deviation of aboveground point heights
skew	Skewness of all point heights
skew.ag	Skewness of aboveground point heights
kurt	Kurtosis of all point heights
kurt.ag	Kurtosis of aboveground point heights
vrd.x.y	Vertical relative point densities between heights x and y: the number of points between x and y divided by the total number of points between 0 and 5 m in height (all points in a given area), for all height ranges between 0 and 5 m at an interval of 0.5 m [[x = 0, y = 0.5], [x = 0.5, y = 1], [...], [x = 4.5, y = 5]]
vnrd.x.y	Vertical normalized relative point densities between heights x and y: the number of the number of points between x and y divided by the number of points between 0 and y (only points within height range and below), for all height ranges between 0 and 5 m at an interval of 0.5 m [[x = 0, y = 0.5], [x = 0.5, y = 1], [...], [x = 4.5, y = 5]]

In addition, a suite of intensity metrics was derived in order to take advantage of the multispectral nature of the ALS data (Table 2).

$$R^2 = 1 - \frac{\sum (y_i - \hat{y}_i)^2}{\sum (y_i - \bar{y})^2} \quad (1)$$

$$RMSE = \sqrt{\frac{\sum (y_i - \hat{y}_i)^2}{n}} \quad (2)$$

$$MAE = \frac{\sum |y_i - \hat{y}_i|}{n} \quad (3)$$

$$bias = \frac{\sum (\hat{y}_i - y_i)}{n} \quad (4)$$

Cross-validation results were compared to the final model results to assess whether or not overfitting occurred.

2.6. Regional-scale AGB modeling (ALS – Landsat/GEDI)

With a well-tuned, local-scale AGB predictive model, we were then able to perform our second, regional-scale analysis. The goal of this portion of the study is to use the modeled results of the local-scale predictive model as reference data to build a regional-scale model, enabling the mapping of woodland AGB throughout the entirety of BENM. There were three main parts to this analysis: (1) comparing ALS-derived AGB to GEDI waveform metrics for regional predictive modeling; (2) comparing ALS-derived AGB to Landsat spectral metrics for regional predictive modeling; and (3) comparing ALS-derived AGB to both GEDI and Landsat metrics for regional predictive modeling. Each part will be described below.

To compare ALS-derived AGB to GEDI data, we acquired GEDI data and conducted all of the following processing steps in R using the rGEDI library (Silva et al., 2020). All GEDI Level 1B (L1B), Level 2A (L2A), and Level 2B (L2B) datasets that overlapped BENM (Fig. 1B) for the entire year of 2019 were acquired. For a comprehensive description of these datasets, please refer to Dubayah et al. (2020). Briefly, the L1B product contains the footprint geolocation information, the L2A product contains waveform relative height metrics, and the L2B product contains derivative structural metrics from the L2A waveform, such as canopy cover and plant area index. In all, data from 39 different dates in 2019 were acquired, totaling 283,312 individual GEDI footprints (Table S1). Although some of the datasets represented winter conditions, which could potentially present complications if there were snow on the ground, a comparison to contemporaneous SNOTEL data from a nearby site suggested that snow did not begin accumulating until after the last GEDI date in 2019. In order to develop a regional-scale model, we needed to compare GEDI metrics to ALS metrics. Accordingly, we needed to create a subset of GEDI footprint points that fell within the local-scale ALS data collection areas (Fig. 1C). To do this, we derived footprint gelocations (as center points) from the L1B product, derived L2A and L2B datasets based on the subset of footprints that fell within the ALS data collection areas ($n = 12,769$). All L2A waveform relative height metrics and L2B structural metrics were derived for each footprint (Table 3). For a complete description of how these metrics are computed, please refer to Luthcke et al. (2019), Hofton and Blair (2019), and Tang and Armston (2019).

Other diagnostic metrics were also retained, not for use as modeling predictors, but for quality filtering, such as the degrade flag and quality flag attributes. Only those unflagged footprints were retained for further analysis, which eliminated approximately 40% of the regional-scale footprints and 24% of the local-scale footprints, leaving 170,512 regional and 9707 local footprints for further analysis. GEDI waveform footprints are approximately 25 m in diameter. Accordingly, in the absence of any positional uncertainty, one could simply subset an ALS

point cloud within a 12.5 m radius circular buffer around the footprint center point to perform an ALS-GEDI comparison. Given the geolocation uncertainty associated with GEDI footprints, however, which is reported to be on the order of 15–20 m for the currently available data (GEDI Science Team, 2020), we can assume that a 12.5 m radius ALS subset would not necessarily align with the true GEDI footprint and associated waveform metrics. We can also assume that, by using a larger radius for extracting ALS data, we would be more likely to overlap the true GEDI footprint location. However, it was unknown precisely what plot radius would be most appropriate for ensuring a maximally-effective ALS-GEDI comparison. We opted to test a series of different plot radii empirically, as follows.

For each radius from 10 to 40 m at an interval of 0.5 m, we created a circular buffer around GEDI footprint center points with that radius. We then extracted ALS point cloud data within each buffer area, and generated the same suite of structural and intensity metrics seen in Tables 1 and 2. Those metrics were used in conjunction with the previously-generated local-scale random forest predictive model to estimate AGB within each footprint area. The data were then split evenly and at random into training and validation datasets. The training dataset was used to develop a regional-scale random forest model using the same variable selection and modeling procedure performed at the local scale, described earlier, except now with the GEDI metrics as predictors (Table 3). The model was then applied to the validation data in order to facilitate a direct comparison between the reference AGB (as modeled by ALS data) and the newly-predicted AGB (as modeled by the GEDI data). It is important to note that, although we are using the term “validation data”, because the validation data themselves are the product of a modeling effort and, as such, have inherent uncertainty, the raw validation results should be evaluated cautiously. In Section 2.8 we describe how we address uncertainty in the validation data to attain a more robust estimate of regional-scale model performance. On each iteration, the variable importance was extracted and compiled to determine which GEDI metrics were best for predicting AGB across the range of radii tested.

A 30 m footprint radius was chosen for use in further investigation. This is partly reflective of the results gleaned from the previous analysis, discussed later, but also partly reflective of some additional spatial considerations (Fig. 4). First, GEDI footprint center points have an along-track separation of 60 m. Accordingly, extracting ALS data within a buffer larger than 30 m would result in some of the same ALS data being used in the prediction of AGB in adjacent GEDI footprints (Fig. 4A). Second, this radius agrees with the reported geolocation uncertainty of the GEDI footprint geolocation (15–20 m). Adding these uncertainty bounds to the nominal footprint radius of 12.5 m, this produces a footprint boundary geolocation uncertainty range of 27.5 m and 32.5 m, the average of which is 30 m (Fig. 4B). Third, a 30 m radius facilitates a direct comparison to the Landsat data, because, like GEDI, Landsat 8 OLI data also have a degree of positional uncertainty (approximately 12 m, per Storey et al., 2014). Thus, it is good practice to use a 3×3 pixel area, rather than a single pixel, as a basis of comparison between reference data and Landsat pixel values (Congalton and Green, 2008). A

Table 2

Plot-level ALS intensity metrics generated from ground height-normalized point cloud data used as predictor variables for local-scale AGB modeling.

Abbreviation	Metric
<i>mi.y</i>	Mean of all point intensities in band y for each of the three bands
<i>mi.y.ag</i>	Mean of aboveground point intensities in band y for each of the three bands
<i>sd.y</i>	Standard deviation of all point intensities in band y for each of the three bands
<i>sd.y.ag</i>	Standard deviation of aboveground point intensities in band y for each of the three bands
<i>pi.y.x</i>	xth intensity percentile of rank-ordered point percentiles from 5th to 100th at a 5 percentile interval in band y for each of the three bands

Table 3

GEDI L2A and L2B metrics generated from geolocated footprints used as predictor variables for regional-scale AGB modeling. For description of how these metrics were derived, please refer to Luthcke et al. (2019), Hofton and Blair (2019), and Tang and Armston (2019).

Product	Abbreviation	Metric
L2A	<i>r_x</i>	Relative waveform height at the <i>x</i> th percentile for every percentile between 0 and 100 at an interval of 1 percentile
L2B	<i>cover</i>	Total canopy cover
L2B	<i>elev.</i>	Elevation of the highest waveform return
L2B	<i>highestreturn.elev.</i>	Elevation of the lowest waveform “mode”, or waveform peak
L2B	<i>lowestmode.fhd.normal</i>	Foliage height diversity index normalized by plant area index
L2B	<i>pai</i>	Plant area index
L2B	<i>pgap.theta</i>	Total gap probability

30 m radius enforces this 3×3 pixel area comparison process (Fig. 4C).

Using this 30 m radius, three regional-scale AGB predictive models were generated: (1) using GEDI data alone; (2) using Landsat data alone; and (3) using a combination of GEDI and Landsat data. The first predictive model was already created in the previously-described iterative process. In order to generate the Landsat-based model, Landsat 8 OLI data were acquired for three different cloud-free dates in 2018: May 8th, representing early growing season conditions, June 25th, representing peak of growing season, and September 13th, representing early senescence. Two Landsat tiles were needed for each date to cover the

entirety of BENM (path 36, rows 33 and 34). The data were processed by the United States Geological Survey Earth Resources Observation and Science Center to surface reflectance using the Land Surface Reflectance Code (LaSRC) algorithm (Vermote et al., 2016). In addition to the raw spectral reflectance data, we also generated a suite of vegetation indices (Table 4). The Landsat modeling procedure mirrored that of GEDI, except Landsat spectral reflectance and vegetation indices, computed as 3×3 pixel mean values surrounding each footprint, were used as predictors of AGB instead of GEDI waveform metrics.

Finally, a regional-scale AGB model was created by combining all of the possible GEDI predictors and all of the Landsat predictor variables together. The same modeling procedure was once again applied. Comparisons of model fit, predictive error, and bias statistics were made between the GEDI-only model, the Landsat-only model, and the GEDI-Landsat combined model. Variable importance between these three models was also compared to reveal which among the three pools of predictor variables was most important for modeling AGB.

Of the three modeling approaches, the Landsat-only approach is the only one that enables direct, study area-wide estimation of total AGB. Although one of GEDI's explicit mission goals is to map vegetation biomass, its discrete, footprint point-based sampling scheme does not enable spatially-exhaustive AGB estimates. There are a number of GEDI upscaling/interpolation techniques that are being applied to overcome this limitation (Dubayah et al., 2020; Saarela et al., 2018), but they are beyond the scope of this study. Thus, to estimate total AGB throughout BENM, we used the Landsat-only predicted values subset to the extent of PJ woodlands within AGB.

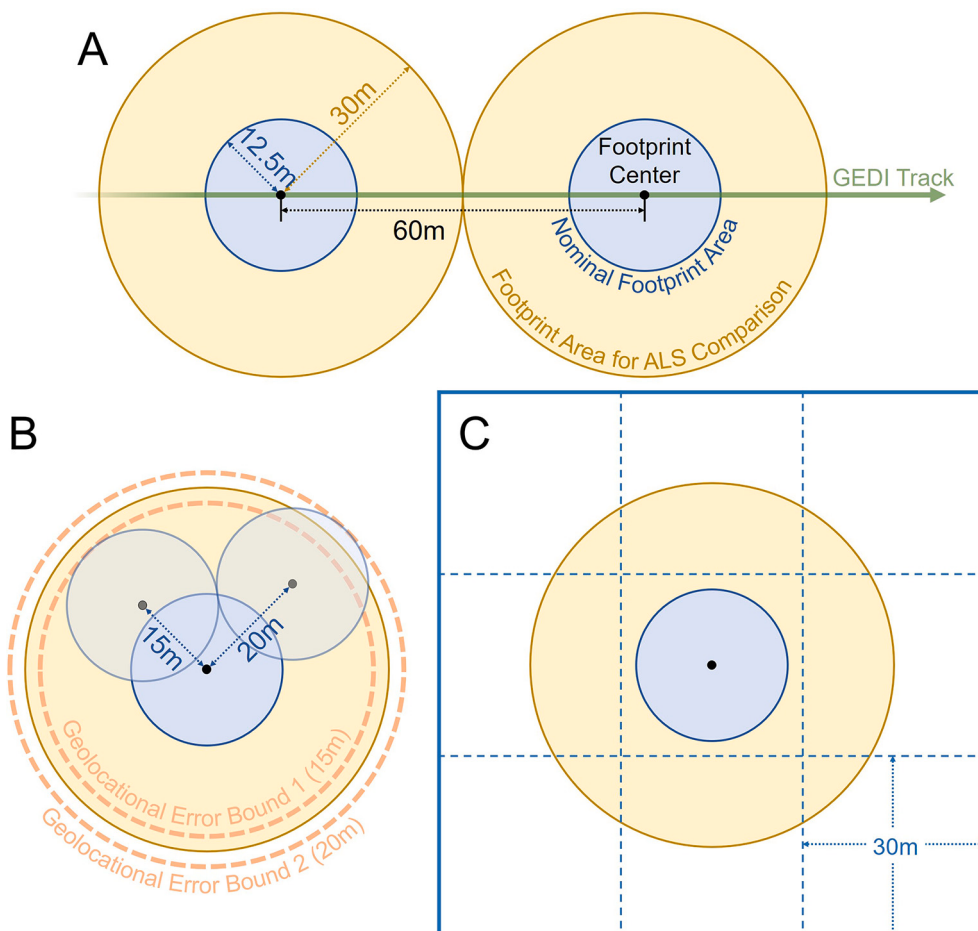


Fig. 4. Justification for selecting 30 m footprint radius: (A) to avoid overlap between sequential GEDI footprints; (B) to fall in between the reported geolocation uncertainty error bounds; and (C) to ensure that 3×3 Landsat pixels are overlapped.

Table 4

Vegetation indices generated from Landsat 8 OLI imagery used as AGB predictor variables in this study, with abbreviations, formula, and sources. SWIR₁ and SWIR₂ are Landsat 8 bands 6 and 7, respectively.

Index	Abbreviation	Formula	Source
Normalized Difference Vegetation Index	NDVI	$\frac{(NIR - Red)}{(NIR + Red)}$	Rouse (1974)
Enhanced Vegetation Index	EVI	$2.5 \times \frac{(NIR - Red)}{(NIR + 6 \times Red - 7.5 \times Blue + 1)}$	Liu and Huete (1995)
Near Infrared Reflectance of Vegetation Soil Adjusted Vegetation Index	NIRv SAVI	$NIR \times NDVI$ $1.5 \times \frac{(NIR - Red)}{(NIR + Red + 0.5)}$	Badgley et al. (2017) Huete (1988)
Modified Soil Adjusted Vegetation Index	MSAVI	$\left(2 \times NIR + 1 - \sqrt{(2 \times NIR + 1)^2 - 8 \times (NIR - Red)} \right) / 2$	Qi et al. (1994)
Normalized Difference Moisture Index	NDMI	$\frac{(NIR - SWIR_1)}{(NIR + SWIR_1)}$	Hardisky et al. (1983)
Normalized Burn Ratio	NBR	$\frac{(NIR - SWIR_2)}{(NIR + SWIR_2)}$	Key and Benson (1999)
Normalized Burn Ratio 2	NBR2	$\frac{(NIR + SWIR_2)}{(SWIR_1 - SWIR_2)}$	Miller and Thode (2007)
Tasseled Cap Brightness	TCB	$0.3029 \times Blue + 0.2786 \times Green + 0.4733 \times Red + 0.5599 \times NIR + 0.5080 \times SWIR_1 + 0.1872 \times SWIR_2$	Baig et al. (2014)
Tasseled Cap Greenness	TCG	$-0.2941 \times Blue - 0.2430 \times Green - 0.5424 \times Red + 0.7276 \times NIR + 0.0713 \times SWIR_1 - 0.1608 \times SWIR_2$	Baig et al. (2014)
Tasseled Cap Wetness	TCW	$0.1511 \times Blue + 0.1973 \times Green + 0.3283 \times Red + 0.3407 \times NIR - 0.7117 \times SWIR_1 - 0.4559 \times SWIR_2$	Baig et al. (2014)

2.7. Testing the role of ancillary data in regional model performance

Although the primary focus of our regional-scale modeling process is a comparison between Landsat and GEDI, it is possible that the incorporation of ancillary spatial data may improve the ability to accurately map AGB. This is particularly true in the PJ woodland ecosystem, where environmental and climate gradients are major drivers of AGB. To explore the extent to which climate and topography affect regional-scale model performance, we acquired a variety of 30-year average climate data from PRISM (PRISM Climate Group, Oregon State University, 2019), including annual and monthly precipitation totals, daily mean, maximum, and minimum temperatures, mean dewpoint temperatures, and minimum and maximum vapor pressure deficits, each of which was generated at a spatial resolution of 800 m. We also acquired 30 m spatial resolution digital elevation model data from the USGS, from which we derived a suite of topographic metrics including elevation, slope, cosine transformation of aspect, sine transformation of aspect, topographic position indices at a range of radii, and topographic wetness index. All of these climate and topographic variables were added as potential predictors to the three regional-scale predictive models (GEDI, Landsat, and GEDI + Landsat) and evaluated for model performance.

2.8. Regional-scale uncertainty analysis

In the three regional-scale models, it is important to consider the compounding error that results from the use of scaled modeling approaches, where the erroneous predictions of one model are used as the reference data for another model (Duncanson et al., 2019). One approach to quantifying the propagation of error is to use the framework proposed by Saatchi et al. (2011), where total error (ϵ_{total}) is computed as the root-sum-square of error estimated in each model (Eq. 1):

$$\epsilon_{total} = \sqrt{\epsilon_{local}^2 + \epsilon_{regional}^2} \quad (5)$$

where ϵ_{local} is a measure of local (scale 1) model error such as MAE, and $\epsilon_{regional}$ is a measure of regional (scale 2) model error in the same units. Although this relatively simple approach to quantifying uncertainty has been applied in similar studies that feature nested, scaled modeling analyses (e.g., Asner et al., 2018, 2013; Saatchi et al., 2011), it is merely an estimate of error, given that the data that we are using for validation purposes are also modeled (rather than measured) data. In the absence of a truly independent validation dataset, it is difficult to provide a robust measure of accuracy or error for our regional-scale model. And

even with an independent, field-measured dataset, the positional uncertainty of GEDI data makes direct comparison between field data and satellite data particularly challenging. However, we can leverage the uncertainty information contained within our local-scale predictive model to estimate the uncertainty of the predictions.

Random forests are an ensemble machine learning tool composed of many individual decision trees (Breiman, 2001). When working in a regression (rather than classification) environment, the predicted values from a random forest represent the mean of predictions among all of the decision trees. By averaging out the results of individual trees, random forests ideally produce more robust predictions that are less subject to noise and outliers than any of the individual decision trees that comprise the forest. However, contained within those trees is the inherent uncertainty of individual predictions. Predictions that are very consistent throughout the forest's decision trees are thought to be made with less uncertainty (higher confidence) and vice versa (Coulston et al., 2016). This is the same principle that underlies quantile regression forests (Meinshausen, 2006; Vaysse and Lagacherie, 2017), and is akin to a prediction interval in parametric statistics (e.g., multiple linear regression). Thus, by calculating the variability of predictions among the individual decision trees, one can estimate prediction uncertainty. Likewise, if random forests are used as the basis of predicting reference data for a subsequent modeling procedure, such as the scaled analysis in this study, then the uncertainty associated with the first model can be propagated through to the second model.

To do this, we performed the following analysis. The local-scale random forest model was generated using 10,000 trees. For each of the three regional-scale models, we randomly selected 100 of those local-scale decision trees. Each decision tree was then used to predict the AGB values for a random subsample of 2000 points from the regional-scale reference data. These points were split equally into training ($n = 1000$) and validation ($n = 1000$). The training data were used to build regional-scale random forest models and the validation data were used to assess model performance. In all, this resulted in 300 models: 100 GEDI models, 100 Landsat models, and 100 GEDI + Landsat models. Each model was used to predict biomass throughout all PJ woodlands in BENM. As a result of this Monte Carlo approach, we could calculate several measures of uncertainty. First, we calculated the mean and standard deviation of the model fit and error metrics associated with each iteration (R^2 , RMSE, MAE). In effect this gave us an estimate not only of the scaled model performance, but also of the uncertainty of that performance metric. Second, we calculated the standard deviation of all of the predictions that resulted from the regional-scale models. This

provided us with a spatially-explicit estimate of uncertainty, as every GEDI footprint or Landsat pixel within BENM was attributed with not only a single predicted value, but also a standard deviation of those predictions. Lastly, in addition to a singular estimate of total AGB within BENM derived from the Landsat-only regional model (described in Section 2.6), this iterative approach allowed us to calculate a range of estimates. To do this, we took the 5th and 95th percentile AGB estimates on a per-pixel basis and derived BENM-wide estimates of these uncertainty bounds.

2.9. Regional-scale spatial autocorrelation analysis

Adjacent GEDI footprints, which were the spatial units that served as the reference data locations for our regional model, can be as close as 60 m to one another. Thus, it is possible in our random selection of training and validation reference points that one of these adjacent points is being used to train a model and the other is being used to assess the accuracy of that model. This violates the assumption of independence between training and validation data, as the proximity of these two points almost certainly means that they are spatially-autocorrelated with respect to AGB (Chen et al., 2019; Ploton et al., 2020). To test the effects of spatial autocorrelation on model performance, we performed a BLOOCV analysis on each of the three regional-scale models, as follows. A random point from the reference data was selected. This point would serve as the leave-one-out validation sample. This point was then buffered by a given distance. A random selection of 1000 other reference points that did not overlap that buffer were used to build a random forest-based AGB predictive model. The model was then applied to the validation point and compared to its reference value. This was repeated 500 times for every buffer distance between 500 m and 20,000 m at an interval of 500 m. Model fit and error metrics (R^2 , RMSE, and MAE) were computed among the 500 iterations at each radius and compared among the range of radii to determine the effect of spatial autocorrelation on model performance.

3. Results

3.1. Local-scale AGB modeling (Field – ALS)

The first of the two modeling scales compared field-based, plot-level estimates of AGB to a suite of ALS structural and intensity metrics in the hopes of being able to predict and map AGB on the local scale. This predictive model was able to account for 74% of variance in AGB, with a RMSE of 14 Mg/ha, a MAE of 11.09 Mg/ha, and a bias of -0.38 Mg/ha (Fig. 5). The cross-validation results were very similar ($R^2_{\text{median}} = 0.73$; $\text{RMSE}_{\text{median}} = 13.79 \text{ Mg/ha}$; $\text{MAE}_{\text{median}} = 10.74 \text{ Mg/ha}$; $\text{bias}_{\text{median}} = -0.54 \text{ Mg/ha}$), suggesting that the model is fairly robust and is not overfitting the data.

The VSURF variable selection procedure resulted in a very parsimonious model, reducing the 124 possible predictor variables down to only four. In order of decreasing variable importance, they are *cd* (canopy density), *vrd.0.50* (vertical relative ALS point density between 0 and 0.5 m in height above the ground), *mh* (mean height of ALS points), and *mi.b2* (mean intensity of band 2) (Fig. 6). Of the four variables, the first three are structural, and only the fourth is intensity-based. Interestingly, the band selected (band 2), which represents intensity in the near-infrared band, is at the wavelength most common to single-wavelength ALS instruments. And the fact that intensity in only one of the three ALS bands in our point cloud data was selected for prediction suggests that the multispectral nature of the ALS dataset did not improve the capacity for AGB mapping.

Unlike traditional regression techniques, random forests are non-parametric in nature, and thus do not produce a model with simple, easily-interpreted coefficients that can provide insight into the magnitude and direction of the relationship between dependent and independent variables. However, one commonly-applied approach to quantifying the nature of those relationships is through the evaluation of

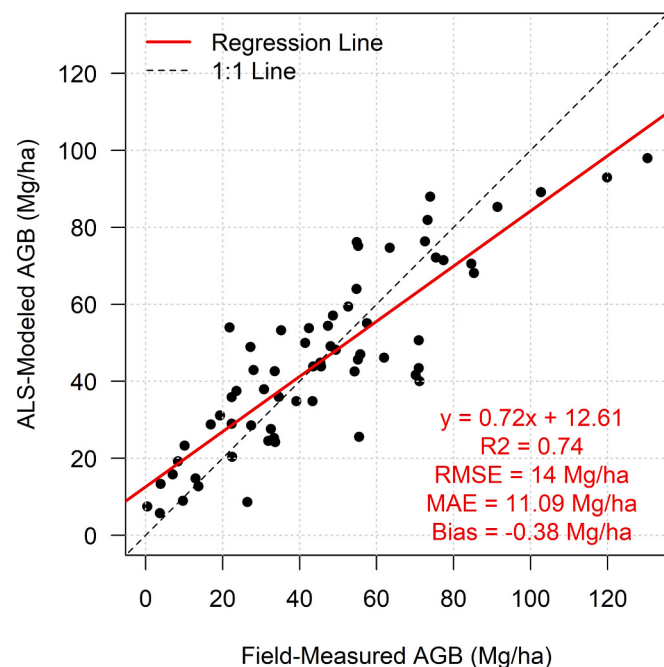


Fig. 5. Results of local-scale AGB modeling, comparing field-measured AGB to ALS-modeled AGB.

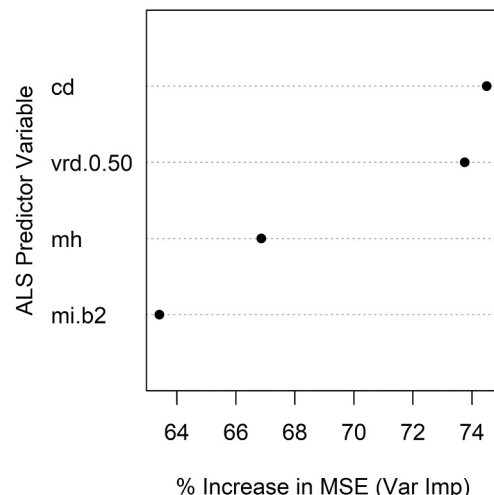


Fig. 6. Local-scale variable importance, as measured by the percent increase in mean squared prediction error (MSE) when a variable is removed from the random forest modeling process. Abbreviations: *cd* = canopy density; *vrd.0.50* = vertical relative ALS point density between 0 and 0.5 m in height above the ground; *mh* = mean height of ALS points; *mi.b2* = mean intensity of band 2.

partial dependence (Cánovas-García et al., 2017). Partial dependence provides insight into the effect of individual predictor variables on the outcome variable while accounting for the effects of the other model predictors (Arribas-Bel et al., 2017). The partial dependence plots for each of the four most important predictor variables in our local-scale model can be seen in Fig. 7. As *cd* increases, so too does AGB, which suggests that a higher density of ALS point returns above breast height is associated with greater AGB. As *vrd.0.50* increases, AGB decreases, meaning that a greater relative proportion of low-lying points is linked to higher AGB totals – this is essentially the inverse of the *cd*-AGB relationship. As *mh* increases, so too does AGB, suggesting that taller vegetation is associated with greater AGB. Lastly, as *mi.b2* increases, AGB decreases. In the passive remote sensing realm, one might expect

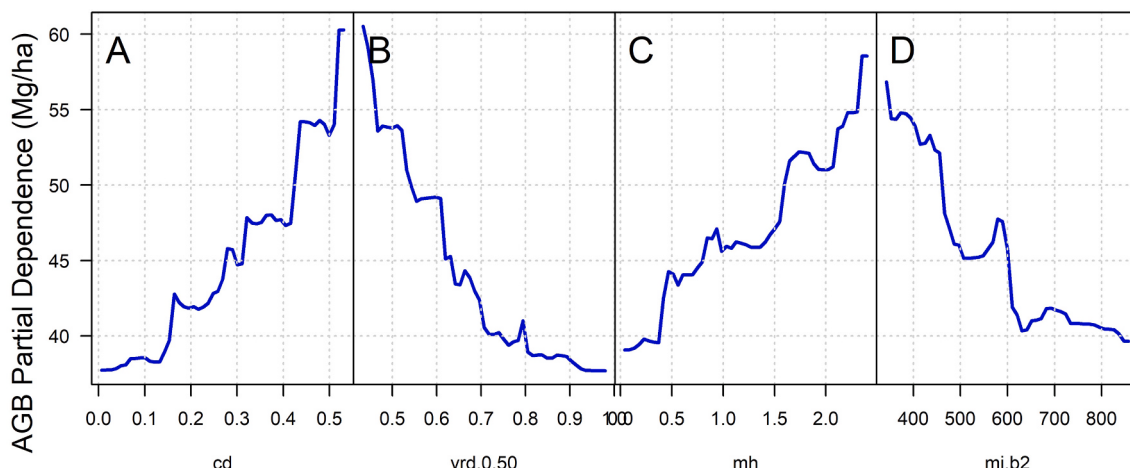


Fig. 7. Partial dependence of the four ALS-derived variables selected for predicting AGB at the local scale. Abbreviations: *cd* = canopy density; *vrd.0.50* = vertical relative ALS point density between 0 and 0.5 m in height above the ground; *mh* = mean height of ALS points; *mi.b2* = mean intensity of band 2.

that higher AGB environments would possess higher near-infrared reflectance, as healthy foliage tends to strongly reflect wavelengths in that range. However, with ALS data, intensities are as much of an indicator of the surface geometry as they are the spectral characteristics of the surface. Thus, pulses interacting with multiple-scattering tree canopies, are more likely to scatter and produce lower return intensities than pulses interacting with the ground surface. Accordingly, more densely vegetated plots with more tree canopy cover, will likely produce lower ALS intensities.

3.2. Regional-scale AGB modeling (ALS – GEDI/Landsat)

The results of the local-scale AGB modeling effort were used as the basis of generating training and validation data for the regional-scale AGB modeling procedure. Three different models were produced, representing AGB predicted using GEDI data alone (Fig. 8A), using Landsat data alone (Fig. 8B), and using a combination of GEDI and Landsat data (Fig. 8C). The GEDI-only model produced the weakest results of the three ($R^2 = 0.68$; RMSE = 10.6 Mg/ha; MAE = 7.87 Mg/ha; bias = 0.04 Mg/ha). The Landsat-only model produced results of intermediate quality ($R^2 = 0.87$; RMSE = 6.86 Mg/ha; MAE = 4.98 Mg/ha; bias = 0.08 Mg/ha). The combined model produced the best results ($R^2 = 0.89$; RMSE = 6.44 Mg/ha; MAE = 4.64 Mg/ha; Bias = 0.08 Mg/ha).

Unlike the local-scale AGB predictive model, where only four variables were selected, the three regional scales produced much more complex models, likely due to the large number of samples used to

generate them and the associated ability to capture much more nuanced relationships between AGB and the predictors (Fig. 9). The GEDI-only model featured high importance of the two elevation variables (*elev.highestreturn* and *elev.lowestnode*), which makes sense in this semiarid region, where low elevations are much hotter and drier and cannot support as much AGB as higher, cooler, moister areas. The third and fourth most important predictor variables were also L2B metrics, suggesting that derivative products tend to be more useful than the more raw relative height data contained within the L2A metrics. Among the relative height metrics, there appears to be bimodal importance, such that high relative heights (e.g., *rh88-rh100*) and low relative heights (e.g., *rh1-rh3*) are important predictors of AGB, whereas intermediate heights are less so. Recall, however, that these results are from only a singular footprint radius (30 m). A more robust look into the variable importance of GEDI metrics that was gleaned from the iterative footprint size test is described later on. With respect to the Landsat-only model, a large number of predictors ($n = 24$) were selected for modeling regional AGB. There is no clear pattern among which image date (early, middle, or late season) was most important, although the selection of important variables from all three dates suggest that there is value in incorporating image data captured in different portions of the growing season. There was a clear pattern among which vegetation indices are most useful for predicting AGB. Specifically, NBR, NBR2, and NDMI make up all of the top 6 most important predictors. This points to the utility of longer wavelengths (near infrared-shortwave infrared) for predicting AGB in PJ woodlands. Although the combined model only slightly outperformed

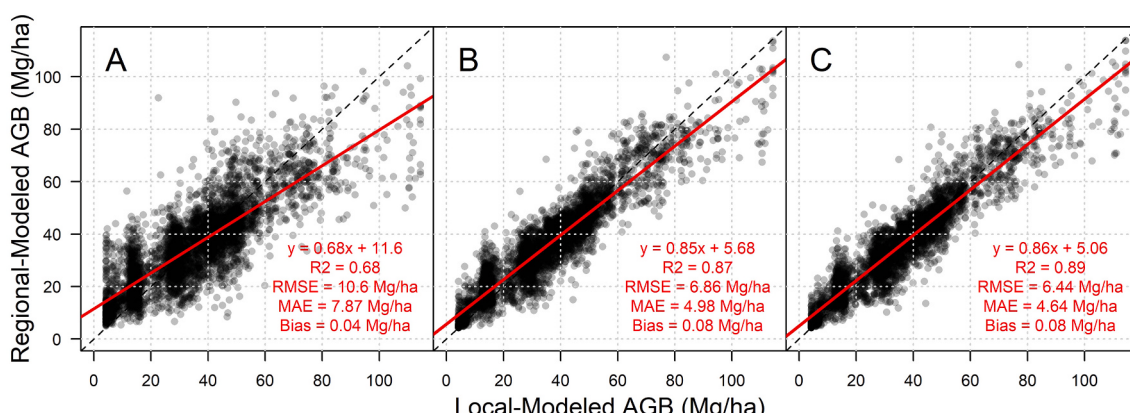


Fig. 8. Results of regional-scale AGB modeling, comparing ALS-modeled AGB to (A) GEDI-modeled AGB, (B) Landsat-modeled AGB, and (C) GEDI and Landsat modeled AGB. Data shown represent the validation dataset.

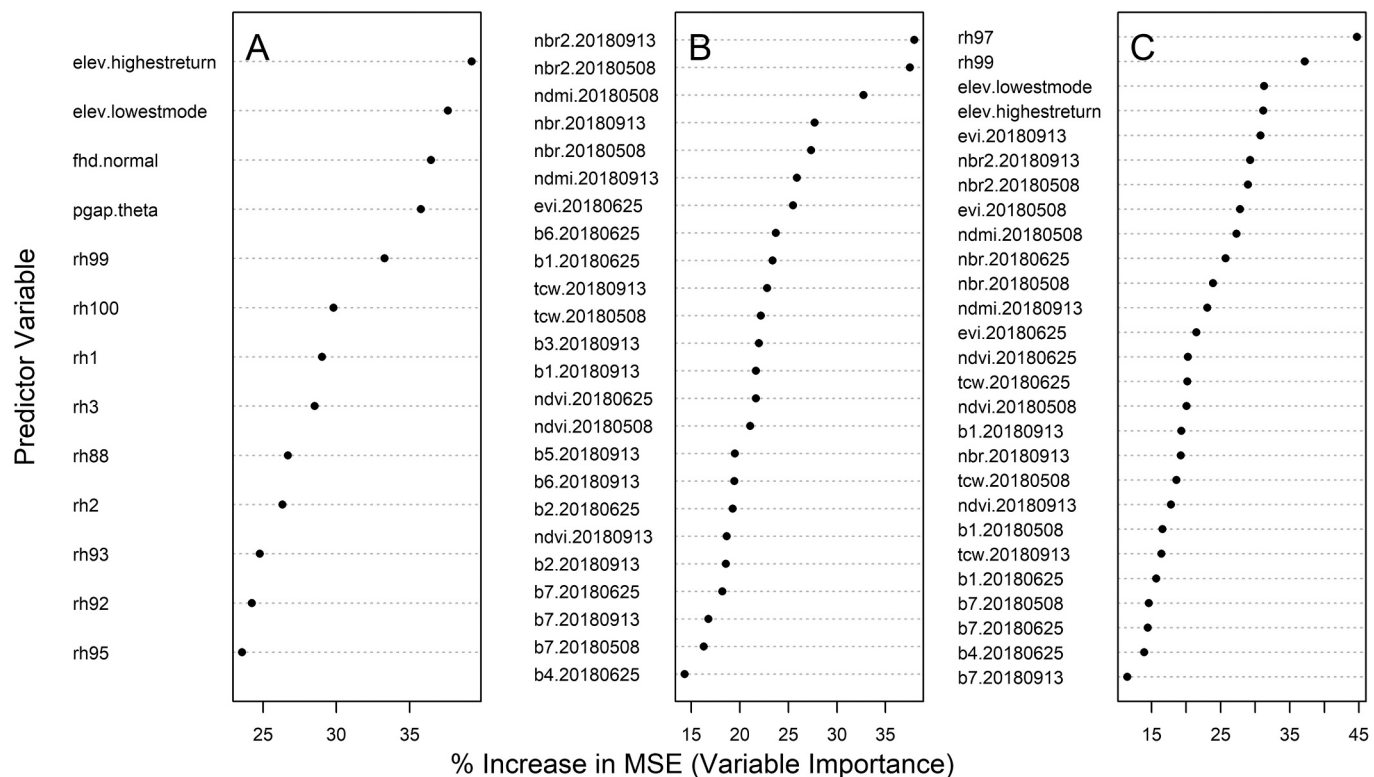


Fig. 9. Regional-scale variable importance, as measured by the percent increase in mean squared prediction error (MSE) when a variable is removed from the random forest modeling process. For variable abbreviations and descriptions, refer to Tables 1, 2, 3, and 4.

the Landsat-only model, clearly the addition of GEDI metrics improved the ability to predict AGB, given that the top four most important variables in the combined model are GEDI metrics.

An example of the application of all of the previously-described AGB predictive models can be seen in Fig. 10. The area shown represents one of the five ALS data extent areas shown in Fig. 1C, featuring a diversity of vegetation and terrain conditions, as evident in the high spatial resolution aerial image in Fig. 10B. The results of the local-scale, ALS-driven model can be seen in Fig. 10C, applied at a 30 m spatial resolution. Note the fact that within the ALS extent there is spatially-exhaustive coverage of AGB estimates, but that limited extent precludes broader-scale AGB estimation. The results of the regional-scale, Landsat-driven model can be seen in Fig. 10D. The general spatial patterns of the Landsat-driven model mirror those of the ALS-driven model, although local-scale AGB variability appears to be lower in the Landsat model. Fig. 10C and E represent the GEDI-only and GEDI/Landsat combined modeling results, respectively. Like the Landsat-only model, AGB can be mapped on a broader, regional basis, but unlike the ALS and Landsat models, the results can only be applied at an individual footprint level. A close examination can reveal subtle differences between the GEDI-only and GEDI/Landsat combined model results, but their overall AGB trends are very similar and are also in line with the ALS and Landsat-only results. As discussed in the Section 2.6, the Landsat-only model is the only model that allows for direct, BENM-wide estimation of AGB. According to LANDFIRE, there is 2734 km² of PJ woodlands in BENM (45% of the entire Monument area). The mean AGB density among these woodlands is 34.38 Mg/ha. When summed throughout BENM, there is an estimated 9.4 Tg of PJ woodland AGB in total.

3.3. GEDI footprint size and variable importance

An empirical comparison of the effect of simulated footprint size on model fit and error can be seen in Fig. 11. The trend is very clear – increasing the footprint size increases the model fit and decreases the

model error. Interestingly, though, the trend is logarithmic, such that the difference in model quality between 10 and 20 m footprint radii is much greater than the difference in model quality between 30 and 40 m footprint radii. Beyond a radius of 30 m, for example, even though the model quality still increases, the increases are minimal. When combined with the additional considerations presented in Fig. 4, this motivated our selection of 30 m as a suitable basis of operation for scaling between ALS, GEDI, and Landsat data.

As mentioned earlier, the iterative nature of the footprint size test yielded 61 separate ALS-GEDI scaling models, each generated using random forests with variable selection. This enabled us to inquire into the variable importance in perhaps a more robust way than a single predictive model, in order to better understand which GEDI metrics are most useful for predicting AGB in woodland ecosystems (Fig. 12). In terms of both the number of times they were selected and their average importance, the two elevation L2B metrics (*elev.highestreturn* and *elev.lowestmode*) were very important for predicting AGB. Again, in this precipitation-limited ecosystem, higher elevation tends to be associated with greater precipitation totals and retention. Similarly, high relative heights (e.g., *rh80-rh100*) tended to show up in a lot of models and have high importance, which makes sense given that taller and denser stands with higher AGB should produce higher relative height metrics. Although low relative heights (e.g., *rh0-rh10*) showed up in a lot of models, their importance was relatively low. This suggests that they are useful for explaining some minor amount of variance in AGB, but their omission would not dramatically alter the model results.

3.4. The role of ancillary data in regional model performance

As can be seen in Fig. 10, the distribution and abundance of vegetation throughout the study area in this region is both spatially-heterogeneous and controlled heavily by abiotic factors, such as topography and climate. Accordingly, when we included climate and topography data into the three regional-scale models, model

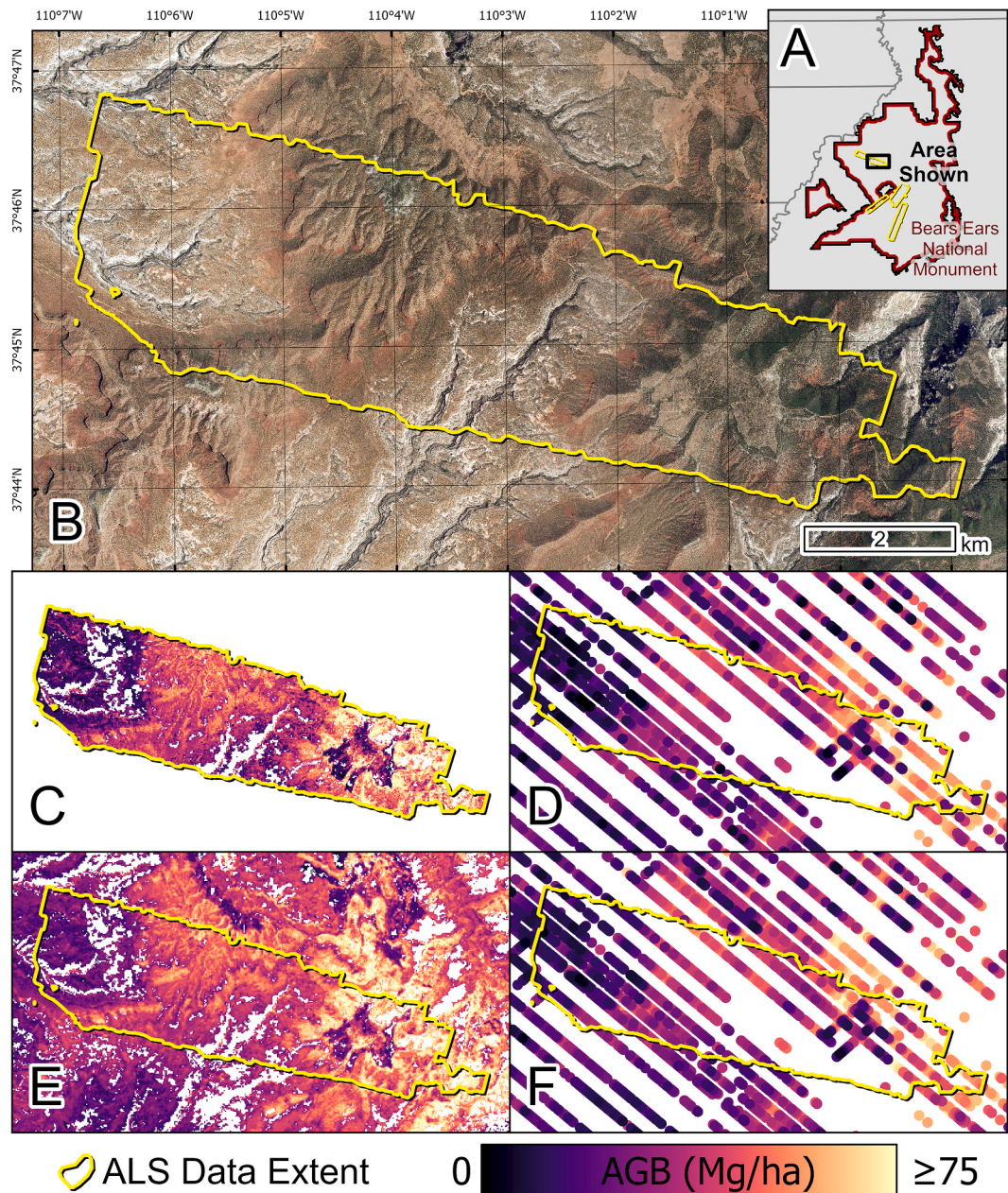


Fig. 10. Example application of local-scale and regional-scale AGB modeling for a portion of the study area featuring diverse terrain and vegetation structure within BENM (A), including an aerial image from the USDA National Agricultural Inventory Program (B), the ALS-modeling results (C), GEDI-only modeling results (D), Landsat-only modeling results (E), and GEDI/Landsat combined modeling results (F). All model results (C–F) are applied only in areas classified as PJ woodlands, according to LANDFIRE ([LANDFIRE, 2020](#)). GEDI footprints (E & F) are enlarged to facilitate visual interpretation.

performance increased. The GEDI-only model saw the greatest improvement in model performance with the inclusion of these ancillary predictors, with the R^2 increasing from 0.69 to 0.80 (16% improvement) and RMSE decreasing from 10.60 Mg/ha to 8.62 Mg/ha (19% improvement). The Landsat-only model saw moderate improvement, with the R^2 increasing from 0.87 to 0.90 (3% improvement) and RMSE decreasing from 6.86 Mg/ha to 6.20 Mg/ha (10% improvement). The combined model saw the least improvement, with the R^2 increasing from 0.89 to 0.90 (1% improvement) and RMSE decreasing from 6.44 Mg/ha to 6.09 Mg/ha (5% improvement).

3.5. Regional-scale uncertainty

We considered regional uncertainty in two ways. The first, relatively simple, albeit statistically-limited approach is using Eq. 5., the results of

which can be seen in Table 5.

The results of the second approach, which used Monte Carlo subsampling of decision trees from the local-scale random forest and propagated their uncertainty through to the reference data of the regional scale models, can be seen in Table 6. Comparing the uncertainty means (ϵ_{mean}) from Table 6 to the total propagated uncertainty estimates (ϵ_{total}) from Table 5 reveals that the relatively simpler root-sum-squared approach for calculating propagated uncertainty results in higher estimates of uncertainty (poorer apparent regional scaled model performance). One benefit of the more nuanced, decision tree-based approach for scaling uncertainty is that it allows for the calculation of standard deviation of the uncertainty metrics (ϵ_{sd}). Taking these into account, we can see that the simpler uncertainty propagation metrics from Table 5 are within 2 standard deviation of the mean propagated RMSE and MAE from Table 6. Another benefit is that it allows for the propagation of

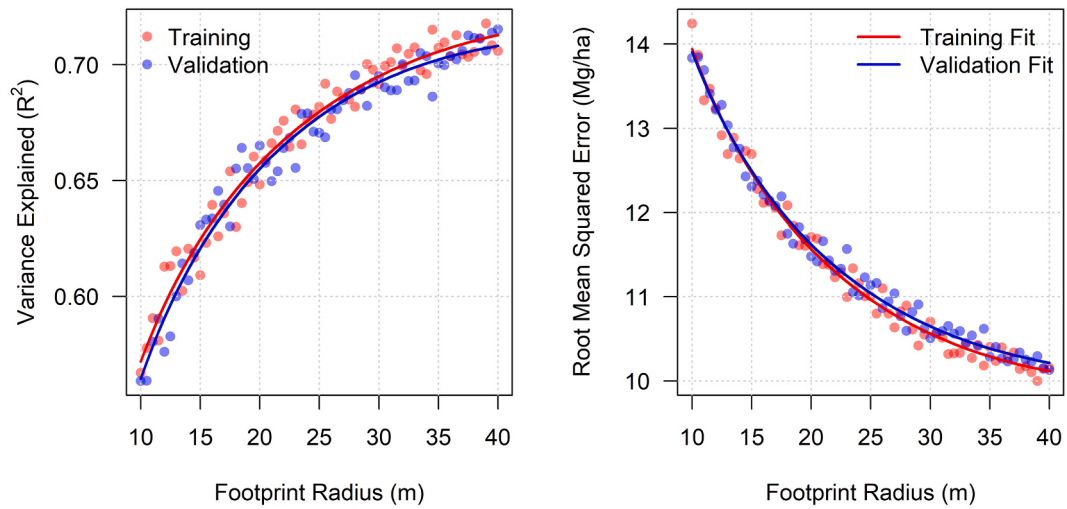


Fig. 11. The effect of footprint size on regional-scale AGB model quality, in terms of variance explained (left) and root mean squared error (right).

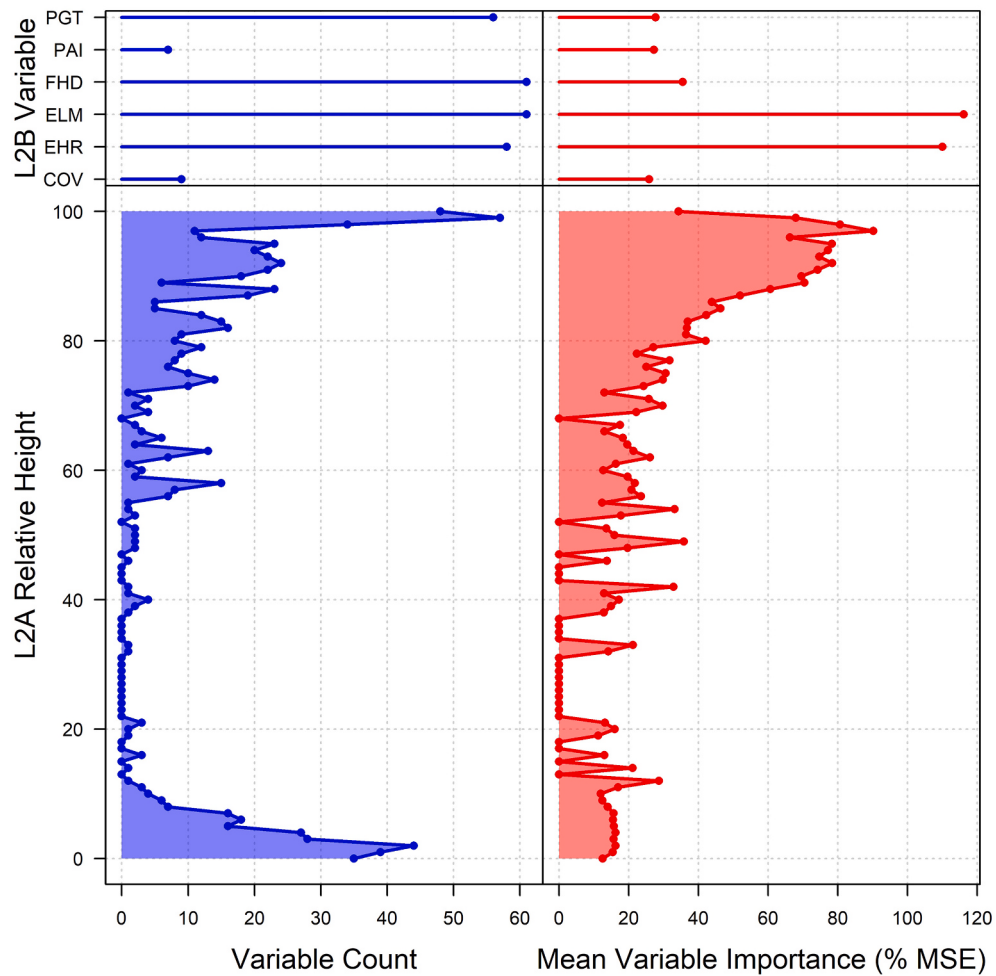


Fig. 12. Aggregated variable importance for GEDI-based regional AGB prediction from the 61 iterations (10–60 m by 0.5 m interval) on different footprint radii, in terms of the number of times variables were selected in the final predictive model (left) and the mean variable importance of those variables (right).

uncertainty in variance explained (R^2), which the room-sum-squared approach from Eq. 5 does not. Given the widespread use of R^2 as a metric for model performance in the AGB mapping literature, this enables more direct comparison between the results of various studies.

A third benefit of the decision tree subsampling approach is that, in

addition to overall model performance metrics, it provides uncertainty estimates at the individual prediction level, as approximated by the standard deviation of predicted values (Fig. 13). Generally, prediction uncertainty is highest in areas with highest predicted AGB, which is to be expected. However, some interesting patterns of uncertainty

Table 5

Results from the first uncertainty propagation analysis for the three regional models based on Eq. 5.

Model	Metric	$\varepsilon_{\text{local}}$ (Mg/ha)	$\varepsilon_{\text{regional}}$ (Mg/ha)	$\varepsilon_{\text{total}}$ (Mg/ha)
GEDI-only	RMSE	14.00	10.60	17.56
	MAE	11.09	7.87	13.60
Landsat-only	RMSE	14.00	6.86	15.59
	MAE	11.09	4.98	12.16
Landsat + GEDI	RMSE	14.00	6.44	15.41
	MAE	11.09	4.64	12.02

Table 6

Results from the second uncertainty propagation analysis for the three regional models based on subsampling of decision trees from the local-scale random forest model, including the mean and standard deviation of uncertainty estimates derived from 100 iterations.

Model	Metric	$\varepsilon_{\text{mean}}$	ε_{sd}
GEDI-only	R ²	0.49	0.06
	RMSE	16.01 Mg/ha	1.6 Mg/ha
	MAE	12.14 Mg/ha	1.28 Mg/ha
Landsat-only	R ²	0.66	0.05
	RMSE	13.08 Mg/ha	1.61 Mg/ha
	MAE	9.71 Mg/ha	1.3 Mg/ha
Landsat + GEDI	R ²	0.68	0.06
	RMSE	12.71 Mg/ha	1.66 Mg/ha
	MAE	9.40 Mg/ha	1.37 Mg/ha

emerged, particularly in the Landsat-only and combined Landsat + GEDI model results (Fig. 13 C & D). A close review of the spatial patterning of uncertainty in comparison to aerial imagery suggested that the background soil reflectance characteristics were driving some of the predictive uncertainty. The high-uncertainty patches in Fig. 13C correspond very closely to the dark red soils seen in the aerial image (Fig. 13A). Cross-referencing with local geologic data reveals that these areas are part of the Moenkopi Formation, which is dominated by reddish-brown mudstone, sandstone, and siltstone. Background soil reflectance is a known challenge in mapping vegetation structure and condition in sparsely-canopied ecosystems such as PJ woodlands (Campbell et al., 2020; Huete, 1988; Qi et al., 1994; Smith et al., 2019). The GEDI-only

model, however, does not appear to be affected by soil color, as evidenced by the lack of correspondence between the spatial distribution of reddish soils in Fig. 13A and predictive uncertainty in Fig. 13B.

Lastly, the iterative approach allows for calculation of uncertainty bounds on total AGB prediction. As discussed in Sections 2.6 and 3.2, the Landsat-only model is the only of the three regional-scale models that allows for direct AGB estimation throughout BENM. Whereas the total AGB estimate from the complete Landsat-only model was 9.4 Tg, the iterative analysis allowed us to compute estimates of the 5th and 95th percentiles of total AGB, which were 7.5 Tg and 12.0 Tg, respectively.

3.6. Regional-scale spatial autocorrelation

The results of the BLOOCV analysis aimed at assessing the effects of spatial autocorrelation on model performance can be seen in Fig. 14. As the buffer distance increases, model performance decreases. In other words, when models are built with training data that are more distant from the data that are being used to validate the model, apparent model quality decreases. This is largely to be expected – calibrating a model in one place and applying it far away will almost always yield worse results than applying it close by. However, even with a buffer distance of 20 km – that is, even when training data and validation data are no closer than 20 km within our study area – the model performance metrics still suggest moderate strength. Particularly in the case of the combined GEDI and Landsat model, even at extreme buffer distances, the R² values are above 0.7. This suggests that our regional modeling procedure is fairly robust to the effects of spatial autocorrelation.

4. Discussion

Here, we leveraged data fusion techniques with Landsat and GEDI to model AGB in woodland ecosystems. We found: (1) Landsat alone is better than GEDI alone; and (2) Landsat and GEDI combined is better than either individually. These results might seem counterintuitive, particularly given the fact that AGB mapping is one of GEDI's main purposes. However, we believe this is attributable to a few possible factors. First, we suspect that the footprint size and waveform sensitivity of GEDI pose challenges for mapping AGB in woodlands with relatively sparse cover and short trees. In such environments, it may be difficult for

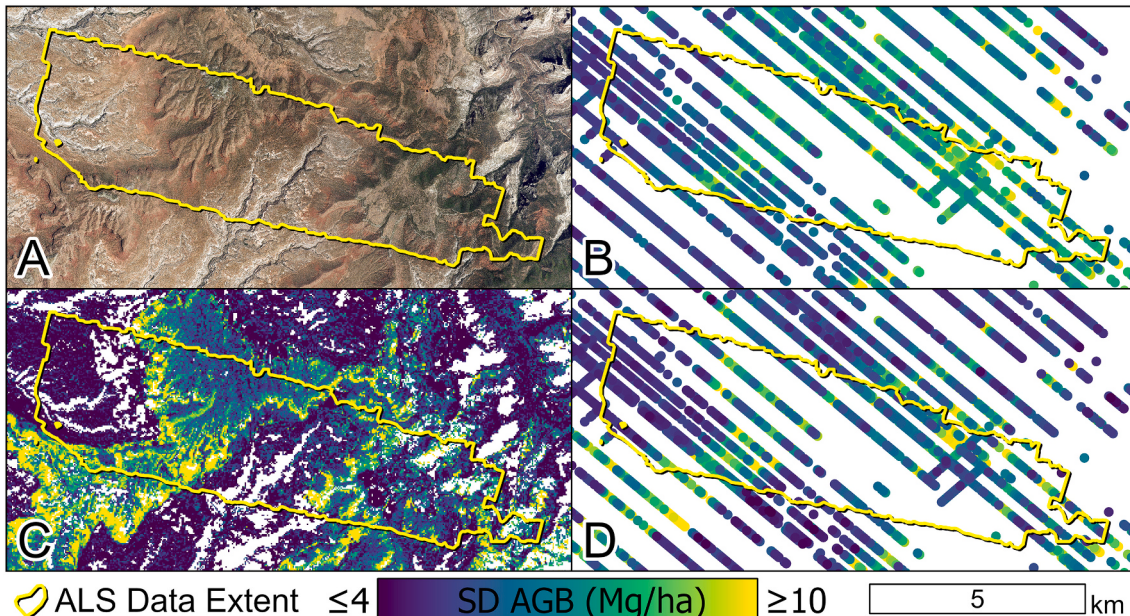


Fig. 13. Example results from the regional-scale AGB uncertainty mapping process depicting the same area as in Fig. 10, including an aerial image (A), the standard deviation of AGB predictions for the GEDI-only model (B), from the Landsat-only model (C), and from the combined GEDI and Landsat model (D).

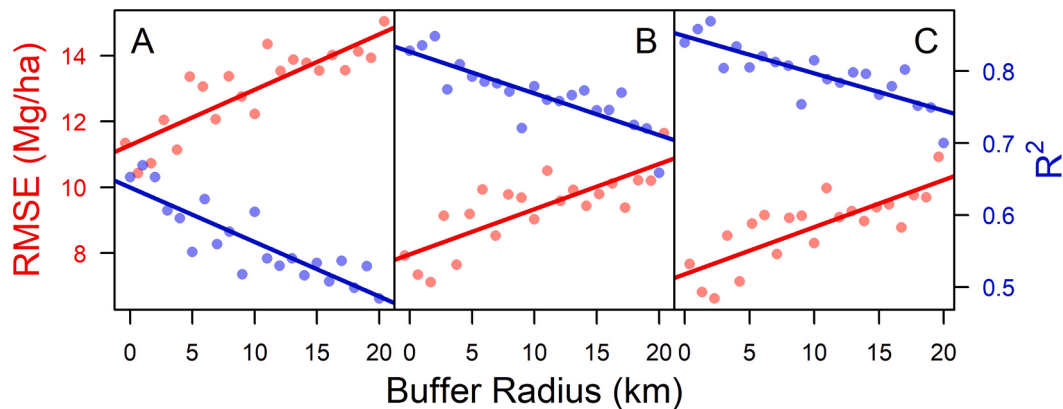


Fig. 14. Results of BLOOCV analysis to determine the effects of spatial autocorrelation on model performance, as approximated by RMSE and R^2 , at a range of buffer radii for regional AGB modeling using GEDI (A), Landsat (B), and GEDI and Landsat (C).

GEDI's algorithms to distinguish between the ground surface and vegetation, particularly in diverse terrain. Further research in similarly-structured ecosystems is required to test this hypothesis. Second, there was a time discrepancy between the three remote sensing datasets used in this study. The ALS and Landsat data were both captured in 2018, making them the most directly comparable. The data from GEDI, due to its launch in late 2018, had to come from the following year, 2019. Although one year should ordinarily have a relatively minimal effect on AGB comparisons, an exceptional drought in this region during 2018 actually triggered a significant mortality event in these woodlands (Campbell et al., 2020; Kannenberg et al., 2021). In this event, nearly 39% of PJ experienced some degree of mortality, with localized patches of high canopy mortality being localized to only approximately 1% of the region. Although woody AGB would not have been altered between 2018 and 2019, significant foliage loss could result in some ALS-GEDI disagreement. It is currently unknown how the presence of an abundance of dead AGB within a GEDI footprint will affect waveform metrics. Future research should aim to explore the relationship between mortality and GEDI-AGB modeling. Lastly, the biomass in piñon and juniper trees is less sensitive to tree height as it is to other biometrics such as stem diameter and crown area (Sprinkle and Klepac, 2015). This acts as a disadvantage to a sensor such as GEDI, whose waveform provides a direct measure of vegetation height, and an advantage to multispectral sensors such as Landsat, whose pixel reflectance is more closely linked to canopy cover rather than canopy height. Accordingly, it is conceivable that in other woodland types that feature trees with greater variability in height, GEDI would outperform Landsat. Even taking these factors into account, GEDI was still able to explain nearly half of regional-scale AGB, factoring in uncertainty propagation from the local scale, which is quite good in comparison to the existing literature (e.g., Huang et al., 2009; Saarela et al., 2018).

The impressive performance of Landsat, both alone and in combination with GEDI data, is also worth noting. It is known that Landsat 8 OLI, and other passive spectral remote sensing sensors, can reach a saturation point in densely-vegetated environments, limiting the capacity for accurate AGB quantification. However, in relatively sparsely-treed woodland ecosystems, this saturation point is likely not met (Huang et al., 2010). In addition, whereas in many forested ecosystems, vegetation height is a good proxy for AGB, the relatively small differences in height between high AGB and low AGB PJ woodlands in particular suggests that multispectral remote sensing, whose measurements are more closely tied to canopy cover rather than canopy height, may be well-suited for woodland AGB mapping. That being said, the relative importance of GEDI metrics in the combined GEDI-Landsat model suggest that a combination of elevation, height, and spectral response provides the best opportunity for accurate AGB quantification. This highlights the importance of our study focusing on woodland

settings. While other studies have demonstrated success in scaled modeling between ALS and satellite data in tropical (Asner et al., 2018; Xu et al., 2017) and boreal (Luther et al., 2019; Zald et al., 2016) environments, our results highlight the relative strengths and weaknesses of different satellite sensors in a structurally-distinct but globally-widespread ecological setting. Our results suggest that longer wavelengths such as those in the shortwave infrared range are useful for quantifying AGB in PJ woodland. The two most important variables in the Landsat-only model were NRB2, one from early growing season and one from late, both of which rely exclusively on Landsat 8 OLI's two shortwave infrared bands (Table 4). This is consistent with previous research that found change in NBR2 to be a good predictor of PJ canopy mortality (Campbell et al., 2020). It also aligns with previous work suggesting that spectral indices based on shorter wavelengths such as NDVI do not perform as well in dryland woodland settings due to their structural complexities (Norris and Walker, 2020; Smith et al., 2019; Yang et al., 2012). The fact that data from multiple Landsat image acquisition dates were present in the final variable selection highlights the importance of accounting for vegetation phenology in the AGB prediction process. Although piñon and juniper trees are evergreen conifers, and thus their spectral characteristics are somewhat consistent throughout a growing season, the high exposure of understory shrubs and grasses through the sparse canopies can have significant effects on spectral response (Norris and Walker, 2020; Smith et al., 2019).

Incorporating GEDI into our regional model provided minimal improvements in accuracy over using Landsat alone. Moderate resolution multispectral data (e.g., Landsat, Sentinel-2) may have similar advantages over GEDI in other open-canopy woodland environments. More work is needed to determine the ranges of structural parameters that produce accurate modeling with Landsat alone versus GEDI or a combination of GEDI and Landsat. While Landsat alone may prove sufficient for open-canopy woodlands, mapping AGB in higher biomass forests is likely to require GEDI or a combination of GEDI and Landsat data.

It is worth considering the results for our local-scale modeling procedure in the context of other studies who have modeled woodland biomass using ALS data under an area-based approach analytical framework. The most directly-comparable, unitless, and frequently-reported statistic for model fit is that of the percent variance explained by the predictive model (R^2). García et al. (2010) modeled AGB in a semiarid Spanish woodland featuring juniper trees using ALS data, and obtained R^2 values between 0.58 and 0.67. Simonson et al. (2012) modeled AGB in the same region using a more recent ALS dataset, attaining an R^2 of 0.53. Wessels et al. (2012) mapped AGB in a South African woodland with R^2 values ranging between 0.75 and 0.82. Wu et al. (2016) modeled AGB in a piñon-juniper-oak woodland ecosystem in eastern Arizona, achieving R^2 values between 0.56 and 0.68, depending on ALS point density. Krofcheck et al. (2016) modeled

equivalent stem diameters, which are the basis of AGB estimates in most allometries, of juniper trees in a woodland ecosystem of central New Mexico, reporting R^2 values of 0.83, although they were quantifying biomass of individual tree clusters, rather than broader-scale plot areas, thus limiting direct comparability to our study. Goldbergs et al. (2018) modeled AGB in an Australian using a combination of individual tree and an area-based approach, which yielded R^2 values between 0.65 and 0.86, depending on the plot size used, though the trees they were studying are much taller than those found in our study area and their heights are directly linked to AGB. Comparing our local-scale modeling results to these studies, we find that our results are at least comparable and, in some cases, better than those in the existing woodland AGB literature ($R^2 = 0.74$).

Nevertheless, there remains a noteworthy amount of variance left unexplained by our local-scale model and those we've cited here, pointing to the inherent challenges associated with modeling AGB in open-canopied, short-treed woodland ecosystems, even with the benefit of high-quality ALS data. We attribute some of this residual error to uncertainties in the allometries used to estimate AGB in woodlands, where the unique structure of trees such as junipers do not fit typical allometric relationships (Chojnacky et al., 2014). The AGB values modeled in our study are relatively high by comparison to other studies who have mapped PJ woodland AGB (e.g., Filippelli et al., 2020; Huang et al., 2010; Hulet et al., 2014). This points to both the importance of allometric equation selection and the inherent variability of PJ woodland structure throughout its wide habitat range. However a comparison to a database that compiles AGB field plot data from a wide variety of sources revealed that, although on the high end of the PJ AGB range, our results are not outside of the range of existing data (Prichard et al., 2019).

Given the paucity of woodland AGB scaling studies in the existing literature, it is difficult to directly compare our regional-scale results in a similar manner. One such scaling study by Huang et al. (2009) linked an AVIRIS-derived estimate of PJ woodland AGB (via regression to canopy cover) to Landsat 7 ETM+ data with an R^2 of 0.52. More recently, Saarela et al. (2018) presented a methodological framework similar to that demonstrated in this study, by linking ALS data to GEDI and Landsat data. They did not present woodland-specific results, although one of their study areas in Colorado did feature plots in PJ woodlands. In that area, they did not provide R^2 values, but they reported relative standard errors between 6.3%–9.1%. In addition, the GEDI data used were simulated from ALS point cloud data, thus representing idealized GEDI waveforms. These factors make direct comparisons to our study difficult.

Beyond the scaling-specific literature there are several studies that have linked field-level data directly to Landsat data. Avitabile et al. (2012) mapped woodland AGB in Uganda using Landsat 5 TM data and achieved R^2 values between 0.78 and 0.85. Karlson et al. (2015) mapped woodland AGB in Burkina Faso by comparing field measurements to a series of Landsat 8 variables using random forests, attaining an R^2 of 0.57. Gizachew et al. (2016) mapped woodland biomass in Tanzania using Landsat 8 data, achieving maximum R^2 values of 0.25. Egberth et al. (2017) mapped woodland AGB in Tanzania using a combination of ALS and Landsat 8 data (though not in a scaling context, per se), and achieved R^2 values of 0.38 and 0.66 for Landsat alone and Landsat with ALS data, respectively. Filippelli et al. (2020) used a combination of National Agricultural Inventory Program (NAIP) and Landsat imagery to model AGB in PJ woodlands on a broad spatial scale, and while they did not report their plot-level AGB model fit, they reported a canopy cover R^2 of 0.75. Without an independent sample of field validation data, we cannot directly compare our model performance with these studies; however, our decision tree-based error propagation procedure provides an estimate of uncertainty that can be cautiously compared. The propagated variance explained ($R^2 = 0.68 \pm 0.06$ SD) falls in line with, and in some cases demonstrates improved results over, existing studies.

It is worth noting that, ignoring the effects of uncertainty propagation, the two Landsat-driven regional-scale models outperformed the

ALS-driven local-scale model. We believe this is attributable to a two primary factors. First, there is a major difference in the sample size between local- and regional-scale models. The local-scale model was driven by 65 field plots, whereas the regional-scale models were driven by thousands of points. Random forest models tend to perform best with large sample sizes (Fassnacht et al., 2014). Second, this larger regional sample allowed for a wider range of geographic conditions to be sampled. By capturing a wider range of vegetation structural and topographic conditions in the regional-scale modeling procedure, a better representation of the study area could be attained, thus allowing for a more robust modeling procedure.

As with all ecologically-focused remote sensing analyses, it is important to consider the role that spatial autocorrelation plays, particularly in the assessment of model performance (Cánoyas-García et al., 2017; Chen et al., 2019; Dale and Fortin, 2002; Griffith and Chun, 2016; Legendre and Fortin, 1989; Ploton et al., 2020). The spatial distribution of GEDI footprints, which formed the geographic basis of our regional-scale reference data, is such that individual footprints can be as close as 60 m from one another. This distance is well within the range of AGB spatial dependence for the ecosystem we are studying. Accordingly, if a sufficient number of these footprints are being incorporated into the reference dataset, it is likely that the assumption of independence between training and validation data is violated. Our application of a BLOOCV analysis (Ploton et al., 2020) demonstrated that, while spatial autocorrelation was indeed affecting our model fit and accuracy metrics, the effects were relatively mild, even at large buffer distances well beyond the range of spatial dependence.

Lastly, our footprint size analysis revealed that using larger simulated footprint areas will increase the accuracy of modeling AGB using GEDI. We attribute this to the positional uncertainty of GEDI footprints, but it also is likely strongly correlated with the structure of the vegetation. Highly spatially heterogeneous vegetation types are more likely to suffer from the effects of GEDI footprint positional inaccuracy, as small shifts in footprint location can result in significant differences in AGB. Conversely, highly spatially homogeneous vegetation types are likely more robust to positional uncertainty. We suspect that across a wide range of vegetation types and structures, the generally positive, asymptotic relationship between footprint size and model accuracy we have demonstrated will persist, but the specific quantitative nature of that relationship will likely differ from one vegetation type to another.

5. Conclusions

In this study, we have presented a framework for modeling and mapping AGB in woodland ecosystems through a flexible and repeatable scaled analytical approach. Improving our capacity for accurately estimating woodland AGB will in turn improve our ability to understand the important role that these ecosystems play in global carbon cycling and land-climate interactions (Ahlström et al., 2015; Bastin et al., 2017; Poulter et al., 2014). The results we have presented provide a sound basis upon which to build future woodland AGB mapping studies and provide insight into the types of data best-suited for quantifying woodland AGB. In PJ, the most abundant woodland type in the US, we found that a combination of satellite multispectral and lidar data produced the most accurate predictions of AGB on a regional scale, outperforming the results of multispectral and lidar data-driven models individually. This suggests that, at least in woodland settings, those attempting to use space-based, waveform lidar for predicting AGB should consider incorporating data from a sensor like Landsat 8 OLI or Sentinel-2. Although we did not test Sentinel-2 data, it is possible that the higher spatial and spectral resolution as compared to Landsat would demonstrate improved results. For example, the GEDI AGB Level 4A product, which will contain footprint-level AGB estimates, would likely benefit from the incorporation of passive reflectance data in its modeling process. Further, in such dryland woodland settings as we have studied here, where the spatial distribution of AGB is heavily controlled by

abiotic factors such as climate and topography, we have demonstrated that the incorporation of such variables into the modeling process can improve predictive power. More research in a diverse range of vegetation types is needed to confirm whether these findings are extensible in a broader range of woodland and other forest settings.

This study also represents an early test case of the application of GEDI data to AGB mapping in woodland ecosystems. The recent launch of the space-based waveform lidar GEDI represents one of the most important steps forward in the effort to map near-global AGB. However, our results found that, while GEDI was able to estimate woodland AGB with a moderate degree of accuracy, Landsat proved superior in this capacity. This stands in contrast to the prevailing paradigm that active remote sensing is better-suited for AGB mapping than passive remote sensing (Zolkos et al., 2013). While that paradigm likely holds true in higher-biomass ecosystems, the unique structure of woodlands clearly necessitates tailored analytical approaches.

Although the combination of Landsat and GEDI resulted in the best performance, the fact that the Landsat-based model performed so well has significant implications. Given that Landsat coverage is both global and spatially-exhaustive, our results suggest that total AGB can be quantified on a per-pixel basis across entire woodland ecosystems. In our study, this allowed us to estimate that BENM, an area of rich with natural and cultural resources that is currently being considered for additional regulatory protection, possesses between 7.5 and 12.0 Tg of woodland AGB (best estimate = 9.4 Tg). These results can be, in turn, compared to spatially-explicit climatic, terrain, and soil variables to assess controls on woodland AGB and facilitate an improved understanding of how future climatic conditions will affect woodland AGB. In addition, the lengthy history of the Landsat archive and projected continuation of the Landsat program presents an added opportunity to quantify losses in AGB over time due to anthropogenic and natural disturbance events, and gains due to growth and recruitment (Wulder et al., 2019; Zhu et al., 2019).

The scaling approach presented in this study hinges upon the ability to link field-measured AGB to ALS at the local scale. There are still large portions of the globe that lack ALS coverage, and while scaling limits the need for exhaustive ALS coverage, to avoid extrapolation, at least a sparse sample of ALS is required. Future research should explore the limitations of using sparse ALS samples as a basis of regional AGB prediction and quantify the effects of extrapolation on AGB model accuracy.

Funding

This research was funded by the National Science Foundation, grant number DEB-1714972.

Declaration of Competing Interest

The authors declare that they have no known competing financial interests or personal relationships that could have appeared to influence the work reported in this paper.

The authors declare the following financial interests/personal relationships which may be considered as potential competing interests.

Appendix A. Supplementary data

Supplementary data to this article can be found online at <https://doi.org/10.1016/j.rse.2021.112511>.

References

- Ahlström, A., Raupach, M.R., Schurgers, G., Smith, B., Arneth, A., Jung, M., Reichstein, M., Canadell, J.G., Friedlingstein, P., Jain, A.K., Kato, E., Poulter, B., Sitch, S., Stocker, B.D., Vivoy, N., Wang, Y.P., Wiltshire, A., Zaehle, S., Zeng, N., 2015. The dominant role of semi-arid ecosystems in the trend and variability of the land CO₂ sink. *Science* 348, 895–899. <https://doi.org/10.1126/science.aaa1668>.
- Arribas-Bel, D., Patino, J.E., Duque, J.C., 2017. Remote sensing-based measurement of living environment deprivation: improving classical approaches with machine learning. *PLoS One* 12, e0176684. <https://doi.org/10.1371/journal.pone.0176684>.
- Askar, N., Phairuang, W., Wicaksana, P., Sayektinginsih, T., 2018. Estimating aboveground biomass on private forest using sentinel-2 imagery. *J. Sens.* <https://doi.org/10.1155/2018/6745629>.
- Asner, G.P., Mascaro, J., Anderson, C., Knapp, D.E., Martin, R.E., Kennedy-Bowdoin, T., van Breugel, M., Davies, S., Hall, J.S., Muller-Landau, H.C., Potvin, C., Sousa, W., Wright, J., Bermingham, E., 2013. High-fidelity national carbon mapping for resource management and REDD+. *Carbon Bal. Manage.* 8, 7. <https://doi.org/10.1186/1750-0680-8-7>.
- Asner, G.P., Brodrick, P.G., Philipson, C., Vaughn, N.R., Martin, R.E., Knapp, D.E., Heckler, J., Evans, L.J., Jucker, T., Goossens, B., Stark, D.J., Reynolds, G., Ong, R., Renneboog, N., Kugan, F., Coomes, D.A., 2018. Mapped aboveground carbon stocks to advance forest conservation and recovery in Malaysian Borneo. *Biol. Conserv.* 217, 289–310. <https://doi.org/10.1016/j.biocon.2017.10.020>.
- Avitabile, V., Baccini, A., Friedl, M.A., Schmullius, C., 2012. Capabilities and limitations of Landsat and land cover data for aboveground woody biomass estimation of Uganda. *Remote Sens. Environ.* 117, 366–380. <https://doi.org/10.1016/j.rse.2011.10.012>.
- Badgley, G., Field, C.B., Berry, J.A., 2017. Canopy near-infrared reflectance and terrestrial photosynthesis. *Sci. Adv.* 3, e1602244 <https://doi.org/10.1126/sciadv.1602244>.
- Baig, M.H.A., Zhang, L., Shuai, T., Tong, Q., 2014. Derivation of a tasseled cap transformation based on Landsat 8 at-satellite reflectance. *Remote Sens. Lett.* 5, 423–431. <https://doi.org/10.1080/2150704X.2014.915434>.
- Bastin, J.-F., Berrahmouni, N., Grainger, A., Maniatis, D., Mollicone, D., Moore, R., Patriarca, C., Picard, N., Sparrow, B., Abraham, E.M., Aloui, K., Atesoglu, A., Attore, F., Bassiliū, Ç., Bey, A., Garzuglia, M., García-Montero, L.G., Groot, N., Guerin, G., Laestadius, L., Lowe, A.J., Mamane, B., Marchi, G., Patterson, P., Rezende, M., Ricci, S., Salcedo, I., Diaz, A.S.-P., Stolle, F., Surappaeva, V., Castro, R., 2017. The extent of forest in dryland biomes. *Science* 356, 635–638. <https://doi.org/10.1126/science.aam6527>.
- Bechtold, W.A., Patterson, P.L. (Eds.), 2005. *The Enhanced Forest Inventory and Analysis Program—National Sampling Design and Estimation Procedures, General Technical Report*. USDA Forest Service, Southern Research Station.
- Bivand, R., Rundel, C., Pebesma, E., Stuetz, R., Hufthammer, K.O., Giraudoux, P., Davis, M., Santilli, S., 2020. rgeos: Interface to Geometry Engine - Open Source ('GEOS').
- Bivand, R., Keitt, T., Rowlingson, B., Pebesma, E., Sumner, M., Hijmans, R., Baston, D., Rouault, E., Warmerdam, F., Ooms, J., Rundel, C., 2021. rgdal: Bindings for the "Geospatial" Data Abstraction Library.
- Breiman, L., 2001. Random forests. *Mach. Learn.* 45, 5–32. <https://doi.org/10.1023/A:1010933404324>.
- Brown, S., 2002. Measuring carbon in forests: current status and future challenges. *Environ. Pollut.* 116, 363–372. [https://doi.org/10.1016/S0269-7491\(01\)00212-3](https://doi.org/10.1016/S0269-7491(01)00212-3).
- Campbell, M.J., Dennison, P.E., Hudak, A.T., Parham, L.M., Butler, B.W., 2018. Quantifying understory vegetation density using small-footprint airborne lidar. *Remote Sens. Environ.* 215, 330–342. <https://doi.org/10.1016/j.rse.2018.06.023>.
- Campbell, M.J., Dennison, P.E., Tunc, J.W., Kannenberg, S.A., Kerr, K.L., Codding, B.F., Anderegg, W.R.L., 2020. A multi-sensor, multi-scale approach to mapping tree mortality in woodland ecosystems. *Remote Sens. Environ.* 245, 111853. <https://doi.org/10.1016/j.rse.2020.111853>.
- Cánovas-García, F., Alonso-Sarría, F., Gomariz-Castillo, F., Oñate-Valdivieso, F., 2017. Modification of the random forest algorithm to avoid statistical dependence problems when classifying remote sensing imagery. *Comput. Geosci.* 103, 1–11. <https://doi.org/10.1016/j.cageo.2017.02.012>.
- Chen, L., Wang, Y., Ren, C., Zhang, B., Wang, Z., 2019. Assessment of multi-wavelength SAR and multispectral instrument data for forest aboveground biomass mapping using random forest kriging. *For. Ecol. Manag.* 447, 12–25. <https://doi.org/10.1016/j.foreco.2019.05.057>.
- Chojnacky, D.C., Rogers, P., 1999. Converting tree diameter measured at root collar to diameter at breast height. *West. J. Appl. For.* 14, 14–16. <https://doi.org/10.1093/wjaf/14.1.14>.
- Chojnacky, D.C., Heath, L.S., Jenkins, J.C., 2014. Updated generalized biomass equations for north American tree species. *Forestry (Lond)* 87, 129–151. <https://doi.org/10.1093/forestry/cpt053>.
- Clark, M.L., Roberts, D.A., Ewel, J.J., Clark, D.B., 2011. Estimation of tropical rain forest aboveground biomass with small-footprint lidar and hyperspectral sensors. *Remote Sens. Environ.* 115, 2931–2942. <https://doi.org/10.1016/j.rse.2010.08.029>.
- DESDynI VEG-3D special issue.
- Clifford, M.J., Royer, P.D., Cobb, N.S., Breshears, D.D., Ford, P.L., 2013. Precipitation thresholds and drought-induced tree die-off: insights from patterns of *Pinus edulis* mortality along an environmental stress gradient. *New Phytol.* 200, 413–421. <https://doi.org/10.1111/nph.12362>.
- Congalton, R.G., Green, K., 2008. *Assessing the Accuracy of Remotely Sensed Data: Principles and Practices*, Second ed. CRC Press.
- Coulston, J.W., Blinn, C.E., Thomas, V.A., Wynne, R.H., 2016. Approximating prediction uncertainty for random forest regression models. *Photogramm. Eng. Remote. Sens.* 82, 189–197. Doi: [10.14358/PERS.82.3.189](https://doi.org/10.14358/PERS.82.3.189).
- Creadon, S., Bergren, E.C., 2019. Bears Ears National Monument: politics, controversy, and potential remedies. *Case Stud. Environ.* 3, 1–9. <https://doi.org/10.1525/cse.2019.001990>.
- Cunliffe, A.M., McIntire, C.D., Boschetti, F., Sauer, K.J., Litvak, M., Anderson, K., Brazier, R.E., 2020. Allometric relationships for predicting aboveground biomass

- and sapwood area of oneseed juniper (*Juniperus monosperma*) trees. *Front. Plant Sci.* 11. <https://doi.org/10.3389/fpls.2020.00094>.
- Cutler, F., Wiener, R., 2018. randomForest: Breiman and Cutler's Random Forests for Classification and Regression.
- Dale, M.R.T., Fortin, M.-J., 2002. Spatial autocorrelation and statistical tests in ecology. *Écoscience* 9, 162–167. <https://doi.org/10.1080/11956860.2002.11682702>.
- Dong, J., Kaufmann, R.K., Myneni, R.B., Tucker, C.J., Kauppi, P.E., Liski, J., Buermann, W., Alexeyev, V., Hughes, M.K., 2003. Remote sensing estimates of boreal and temperate forest woody biomass: carbon pools, sources, and sinks. *Remote Sens. Environ.* 84, 393–410. [https://doi.org/10.1016/S0034-4257\(02\)00130-X](https://doi.org/10.1016/S0034-4257(02)00130-X).
- Drake, J.B., Dubayah, R.O., Clark, D.B., Knox, R.G., Blair, J.B., Hofton, M.A., Chazdon, R.L., Weishampel, J.F., Prince, S., 2002. Estimation of tropical forest structural characteristics using large-footprint lidar. *Remote Sens. Environ.* Recent Adv. *Remote Sens. Biophys. Var.* 79, 305–319. [https://doi.org/10.1016/S0034-4257\(01\)00281-4](https://doi.org/10.1016/S0034-4257(01)00281-4).
- Dubayah, R., Blair, J.B., Goetz, S., Fatoyinbo, L., Hansen, M., Healey, S., Hofton, M., Hurt, G., Kellner, J., Luthcke, S., Armston, J., Tang, H., Duncanson, L., Hancock, S., Jantz, P., Marsalis, S., Patterson, P.L., Qi, W., Silva, C., 2020. The Global Ecosystem Dynamics Investigation: high-resolution laser ranging of the Earth's forests and topography. *Sci. Remote Sens.* 1, 100002. <https://doi.org/10.1016/j.srs.2020.100002>.
- Dubayah, R.O., Sheldon, S.L., Clark, D.B., Hofton, M.A., Blair, J.B., Hurt, G.C., Chazdon, R.L., 2010. Estimation of tropical forest height and biomass dynamics using lidar remote sensing at La Selva, Costa Rica. *J. Geophys. Res. Biogeosci.* 115 <https://doi.org/10.1029/2009JG000933>.
- Duncanson, L., Armston, J., Disney, M., Avitabile, V., Barbier, N., Calders, K., Carter, S., Chave, J., Herold, M., Crowther, T.W., Falkowski, M., Kellner, J.R., Labrière, N., Lucas, R., MacBean, N., McRoberts, R.E., Meyer, V., Næsset, E., Nickeson, J.E., Paul, K.I., Phillips, O.L., Réjou-Méchain, M., Román, M., Roxburgh, S., Saatchi, S., Schepaschenko, D., Scipal, K., Siqueira, P.R., Whitehurst, A., Williams, M., 2019. The importance of consistent global forest aboveground biomass product validation. *Surv. Geophys.* 40, 979–999. <https://doi.org/10.1007/s10712-019-09538-8>.
- Duncanson, L., Neuenschwander, A., Hancock, S., Thomas, N., Fatoyinbo, T., Simard, M., Silva, C.A., Armston, J., Luthcke, S.B., Hofton, M., Kellner, J.R., Dubayah, R., 2020. Biomass estimation from simulated GEDI, ICESat-2 and NISAR across environmental gradients in Sonoma County, California. *Remote Sens. Environ.* 242, 111779. <https://doi.org/10.1016/j.rse.2020.111779>.
- Eggerth, M., Nyberg, G., Næsset, E., Gobakken, T., Mauya, E., Malimbwi, R., Katani, J., Chamuya, N., Bulenga, G., Olsson, H., 2017. Combining airborne laser scanning and Landsat data for statistical modeling of soil carbon and tree biomass in Tanzanian Miombo woodlands. *Carbon Bal. Manag.* 12, 8. <https://doi.org/10.1186/s13021-017-0076-y>.
- Evans, J.S., Murphy, M.A., 2019. rfUtilities: Random Forests Model Selection and Performance Evaluation.
- Fassnacht, F.E., Hartig, F., Latifi, H., Berger, C., Hernández, J., Corvalán, P., Koch, B., 2014. Importance of sample size, data type and prediction method for remote sensing-based estimations of aboveground forest biomass. *Remote Sens. Environ.* 154, 102–114. <https://doi.org/10.1016/j.rse.2014.07.028>.
- Filippelli, S.K., Falkowski, M.J., Hudak, A.T., Fekety, P., Vogeler, J.C., Khalayani, A.H., Rau, B.M., Strand, E.K., 2020. Monitoring pinyon-juniper cover and aboveground biomass across the Great Basin. *Environ. Res. Lett.* <https://doi.org/10.1088/1748-9326/ab6785>.
- Foody, G.M., Boyd, D.S., Cutler, M.E.J., 2003. Predictive relations of tropical forest biomass from Landsat TM data and their transferability between regions. *Remote Sens. Environ.* 85, 463–474. [https://doi.org/10.1016/S0034-4257\(03\)00039-7](https://doi.org/10.1016/S0034-4257(03)00039-7).
- García, M., Riaño, D., Chuvieco, E., Danson, F.M., 2010. Estimating biomass carbon stocks for a Mediterranean forest in Central Spain using LiDAR height and intensity data. *Remote Sens. Environ.* 114, 816–830. <https://doi.org/10.1016/j.rse.2009.11.021>.
- GEDI Science Team, 2020. Global Ecosystem Dynamics Investigation (GEDI) Level 1B User Guide for SDPS PGEVersion 3 (P003) of GEDI L1B Data.
- Genuer, R., Poggi, J.-M., Tuleau-Malot, C., 2015. VSURF: an R package for variable selection using random forests. *R J.* 7, 19–33.
- Gibbs, H.K., Brown, S., Niles, J.O., Foley, J.A., 2007. Monitoring and estimating tropical forest carbon stocks: making REDD a reality. *Environ. Res. Lett.* 2, 045023 <https://doi.org/10.1088/1748-9326/2/4/045023>.
- Gizachew, B., Solberg, S., Næsset, E., Gobakken, T., Bollandsås, O.M., Breidenbach, J., Zahabu, E., Mauya, E.W., 2016. Mapping and estimating the total living biomass and carbon in low-biomass woodlands using Landsat 8 CDR data. *Carbon Bal. Manage.* 11, 13. <https://doi.org/10.1186/s13021-016-0055-8>.
- Goetz, S., Dubayah, R., 2011. Advances in remote sensing technology and implications for measuring and monitoring forest carbon stocks and change. *Carbon Manage.* 2, 231–244. <https://doi.org/10.4155/cmt.11.18>.
- Goldbergs, G., Levick, S.R., Lawes, M., Edwards, A., 2018. Hierarchical integration of individual tree and area-based approaches for savanna biomass uncertainty estimation from airborne LiDAR. *Remote Sens. Environ.* 205, 141–150. <https://doi.org/10.1016/j.rse.2017.11.010>.
- Grier, C.C., Elliott, K.J., McCullough, D.G., 1992. Biomass distribution and productivity of *Pinus edulis*—*Juniperus monosperma* woodlands of north-Central Arizona. *For. Ecol. Manag.* 50, 331–350. [https://doi.org/10.1016/0378-1127\(92\)90346-B](https://doi.org/10.1016/0378-1127(92)90346-B).
- Griffith, D.A., Chun, Y., 2016. Spatial autocorrelation and uncertainty associated with remotely-sensed data. *Remote Sens.* 8, 535. <https://doi.org/10.3390/rs8070535>.
- Hardisky, M., Klemas, V., Smart, R., 1983. Close the influence of soil salinity, growth form and leaf moisture on the spectral radiance of *Spartina alterniflora* canopies. *Photogramm. Eng. Remote. Sens.* 49, 77–83.
- Hijmans, R.J., van Etten, J., 2014. raster: Geographic data analysis and modeling. In: R Package Version 2, p. 15.
- Hofton, M., Blair, J.B., 2019. Algorithm Theoretical Basis Document (ATBD) for GEDI Transmit and Receive Waveform Processing for L1 and L2 Products, Version 1.0. NASA, Goddard Space Flight Center.
- Hollaas, M., Wagner, W., Eberhofer, C., Karel, W., 2006. Accuracy of large-scale canopy heights derived from LiDAR data under operational constraints in a complex alpine environment. *ISPRS J. Photogramm. Remote Sens.* 60, 323–338. <https://doi.org/10.1016/j.isprsjprs.2006.05.002>.
- Hopkinson, C., Chasmer, L., Gynan, C., Mahoney, C., Sitar, M., 2016. Multisensor and multispectral LiDAR characterization and classification of a forest environment. *Can. J. Remote. Sens.* 42, 501–520. <https://doi.org/10.1080/07038992.2016.1196584>.
- Huang, C., Asner, G.P., Martin, R.E., Barger, N.N., Neff, J.C., 2009. Multiscale analysis of tree cover and aboveground carbon stocks in pinyon-juniper woodlands. *Ecol. Appl.* 19, 668–681. <https://doi.org/10.1890/07-2103.1>.
- Huang, C., Asner, G.P., Barger, N.N., Neff, J.C., Floyd, M.L., 2010. Regional aboveground live carbon losses due to drought-induced tree dieback in piñon-juniper ecosystems. *Remote Sens. Environ.* 114, 1471–1479. <https://doi.org/10.1016/j.rse.2010.02.003>.
- Hudak, A.T., Lefsky, M.A., Cohen, W.B., Berterretche, M., 2002. Integration of lidar and Landsat ETM+ data for estimating and mapping forest canopy height. *Remote Sens. Environ.* 82, 397–416. [https://doi.org/10.1016/S0034-4257\(02\)00056-1](https://doi.org/10.1016/S0034-4257(02)00056-1).
- Hudak, A.T., Strand, E.K., Vierling, L.A., Byrne, J.C., Eitel, J.U.H., Martinuzzi, S., Falkowski, M.J., 2012. Quantifying aboveground forest carbon pools and fluxes from repeat LiDAR surveys. *Remote Sens. Environ.* 123, 25–40. <https://doi.org/10.1016/j.rse.2012.02.023>.
- Huete, A.R., 1988. A soil-adjusted vegetation index (SAVI). *Remote Sens. Environ.* 25, 295–309. [https://doi.org/10.1016/0034-4257\(88\)90106-X](https://doi.org/10.1016/0034-4257(88)90106-X).
- Hulet, A., Roundy, B.A., Petersen, S.L., Bunting, S.C., Jensen, R.R., Roundy, D.B., 2014. Utilizing National Agriculture Imagery Program data to estimate tree cover and biomass of piñon and juniper woodlands. *Rangel. Ecol. Manag.* 67, 563–572. <https://doi.org/10.2111/REM-D-13-00044.1>.
- Kankare, V., Vastaranta, M., Holopainen, M., Räty, M., Yu, X., Hyppä, J., Hyppä, H., Alho, P., Viitala, R., 2013. Retrieval of forest aboveground biomass and stem volume with airborne scanning LiDAR. *Remote Sens.* 5, 2257–2274. <https://doi.org/10.3390/rs502257>.
- Kannenberg, S.A., Driscoll, A.W., Malesky, D., Anderegg, W.R.L., 2021. Rapid and surprising dieback of Utah juniper in the southwestern USA due to acute drought stress. *For. Ecol. Manag.* 480, 118639. <https://doi.org/10.1016/j.foreco.2020.118639>.
- Karlson, M., Ostwald, M., Reese, H., Sanou, J., Tankoano, B., Mattsson, E., 2015. Mapping tree canopy cover and aboveground biomass in Sudan-Saharan woodlands using Landsat 8 and random forest. *Remote Sens.* 7, 10017–10041. <https://doi.org/10.3390/rs70801017>.
- Key, C.H., Benson, N.C., 1999. The Normalized Burn Ratio (NBR): A Landsat TM Radiometric Measure of Burn Severity. United States Geological Survey, Northern Rocky Mountain Science Center, Bozeman, MT.
- Korhonen, L., Korpela, I., Heiskanen, J., Maltamo, M., 2011. Airborne discrete-return LiDAR data in the estimation of vertical canopy cover, angular canopy closure and leaf area index. *Remote Sens. Environ.* 115, 1065–1080. <https://doi.org/10.1016/j.rse.2010.12.011>.
- Krofcheck, D.J., Eitel, J.U.H., Vierling, L.A., Schulthess, U., Hilton, T.M., Dettweiler-Robinson, E., Pendleton, R., Litvak, M.E., 2014. Detecting mortality induced structural and functional changes in a piñon-juniper woodland using Landsat and RapidEye time series. *Remote Sens. Environ.* 151, 102–113. <https://doi.org/10.1016/j.rse.2013.11.009>. Special Issue on 2012 ForestSAT.
- Krofcheck, D.J., Litvak, M.E., Lippitt, C.D., Neuenschwander, A., 2016. Woody biomass estimation in a southwestern U.S. juniper savanna using LiDAR-derived clumped tree segmentation and existing allometries. *Remote Sens.* 8, 453. <https://doi.org/10.3390/rs8060453>.
- LANDFIRE, 2020. LANDFIRE Remap 2016 Existing Vegetation Type (EVT) CONUS.
- Lefsky, M.A., Cohen, W.B., Harding, D.J., Parker, G.G., Acker, S.A., Gower, S.T., 2002. Lidar remote sensing of above-ground biomass in three biomes. *Glob. Ecol. Biogeogr.* 11, 393–399. <https://doi.org/10.1046/j.1466-822x.2002.00303.x>.
- Legendre, P., Fortin, M.J., 1989. Spatial pattern and ecological analysis. *Vegetatio* 80, 107–138. <https://doi.org/10.1007/BF00048036>.
- Li, X., Du, H., Mao, F., Zhou, G., Chen, L., Xing, L., Fan, W., Xu, X., Liu, Y., Cui, L., Li, Y., Zhu, D., Liu, T., 2018. Estimating bamboo forest aboveground biomass using EnKF-assimilated MODIS LAI spatiotemporal data and machine learning algorithms. *Agric. For. Meteorol.* 256–257, 445–457. <https://doi.org/10.1016/j.agrformet.2018.04.002>.
- Liu, H.Q., Huete, A., 1995. A feedback based modification of the NDVI to minimize canopy background and atmospheric noise. *IEEE Trans. Geosci. Remote Sens.* 33, 457–465. <https://doi.org/10.1109/TGRS.1995.8746027>.
- Lu, D., 2006. The potential and challenge of remote sensing-based biomass estimation. *Int. J. Remote Sens.* 27, 1297–1328. <https://doi.org/10.1080/0143160500486732>.
- Lu, D., Chen, Q., Wang, G., Moran, E., Batistella, M., Zhang, M., Vaglio Laurin, G., Saah, D., 2012. Aboveground forest biomass estimation with Landsat and LiDAR data and uncertainty analysis of the estimates. *Int. J. For. Res.* 2012, e436537. <https://doi.org/10.1155/2012/436537>.
- Luo, S., Wang, C., Xi, X., Nie, S., Fan, X., Chen, H., Ma, D., Liu, J., Zou, J., Lin, Y., Zhou, G., 2019. Estimating forest aboveground biomass using small-footprint full-waveform airborne LiDAR data. *Int. J. Appl. Earth Obs. Geoinf.* 83, 101922. <https://doi.org/10.1016/j.jag.2019.101922>.
- Luthcke, S.B., Rebold, T., Thomas, T., Pennington, T., 2019. Algorithm Theoretical Basis Document (ATBD) for GEDI Waveform Geolocation for L1 and L2 Products, version 1.0. NASA, Goddard Space Flight Center.

- Luther, J.E., Fournier, R.A., van Lier, O.R., Bujold, M., 2019. Extending ALS-based mapping of forest attributes with medium resolution satellite and environmental data. *Remote Sens.* 11, 1092. <https://doi.org/10.3390/rs11091092>.
- Matasci, G., Hermosilla, T., Wulder, M.A., White, J.C., Coops, N.C., Hobart, G.W., Zald, H.S.J., 2018. Large-area mapping of Canadian boreal forest cover, height, biomass and other structural attributes using Landsat composites and lidar plots. *Remote Sens. Environ.* 209, 90–106. <https://doi.org/10.1016/j.rse.2017.12.020>.
- Meinshausen, N., 2006. Quantile Regression Forests. *J. Mach. Learn. Res.* 7.
- Miller, E.L., Meeuwig, R.O., Budy, J.D., 1981. Biomass of Singleleaf Pinyon and Utah Juniper. *Res. Pap. INT-273*, 18. U.S. Department of Agriculture, Forest Service, Intermountain Forest and Range Experiment Station, Ogden, UT, p. 273. <https://doi.org/10.2737/INT-RP-273>.
- Miller, J.D., Thode, A.E., 2007. Quantifying burn severity in a heterogeneous landscape with a relative version of the delta normalized burn ratio (dNBR). *Remote Sens. Environ.* 109, 66–80. <https://doi.org/10.1016/j.rse.2006.12.006>.
- Mitchard, E.T.A., Flintrop, C.M., 2013. Woody encroachment and forest degradation in sub-Saharan Africa's woodlands and savannas 1982–2006. *Philos. Trans. Roy. Soc. B: Biol. Sci.* 368, 20120406 <https://doi.org/10.1098/rstb.2012.0406>.
- Muukkonen, P., Heiskanen, J., 2005. Estimating biomass for boreal forests using ASTER satellite data combined with standwise forest inventory data. *Remote Sens. Environ.* 99, 434–447. <https://doi.org/10.1016/j.rse.2005.09.011>.
- Næsset, E., 2002. Predicting forest stand characteristics with airborne scanning laser using a practical two-stage procedure and field data. *Remote Sens. Environ.* 80, 88–99. [https://doi.org/10.1016/S0034-4257\(01\)00290-5](https://doi.org/10.1016/S0034-4257(01)00290-5).
- Næsset, E., Gobakken, T., 2008. Estimation of above- and below-ground biomass across regions of the boreal forest zone using airborne laser. *Remote Sens. Environ.* 112, 3079–3090. <https://doi.org/10.1016/j.rse.2008.03.004>.
- Narine, L.L., Popescu, P., Malambo, L., 2019. Synergy of ICESat-2 and Landsat for mapping forest aboveground biomass with deep learning. *Remote Sens.* 11, 1503. <https://doi.org/10.3390/rs1121503>.
- Nguyen, T.H., Jones, S.D., Soto-Berelov, M., Haywood, A., Hislop, S., 2020. Monitoring aboveground forest biomass dynamics over three decades using Landsat time-series and single-date inventory data. *Int. J. Appl. Earth Obs. Geoinf.* 84, 101952. <https://doi.org/10.1016/j.jag.2019.101952>.
- Nordhaus, H., 2021. Biden Set to Restore Bears Ears, Grand Staircase-Escalante to Pre-Trump Size [WWW Document]. National Geographic. URL <https://www.nationalgeographic.com/environment/article/biden-expected-to-reverse-trump-order-to-shrink-utah-national-monuments> (accessed 2.18.21).
- Norris, J.R., Walker, J.J., 2020. Solar and sensor geometry, not vegetation response, drive satellite NDVI phenology in widespread ecosystems of the western United States. *Remote Sens. Environ.* 249, 112013. <https://doi.org/10.1016/j.rse.2020.112013>.
- Okin, G.S., Roberts, D.A., Murray, B., Okin, W.J., 2001. Practical limits on hyperspectral vegetation discrimination in arid and semiarid environments. *Remote Sens. Environ.* 77, 212–225. [https://doi.org/10.1016/S0034-4257\(01\)00207-3](https://doi.org/10.1016/S0034-4257(01)00207-3).
- Flugmacher, D., Cohen, W.B., Kennedy, R.E., Yang, Z., 2014. Using Landsat-derived disturbance and recovery history and lidar to map forest biomass dynamics. *Remote Sens. Environ.* 151, 124–137. <https://doi.org/10.1016/j.rse.2013.05.033>. Special Issue on 2012 Forest SAT.
- Ploton, P., Mortier, F., Réjou-Méchain, M., Barbier, N., Picard, N., Rossi, V., Dormann, C., Cornu, G., Viennois, G., Bayol, N., Lyapustin, A., Gourlet-Fleury, S., Pélassier, R., 2020. Spatial validation reveals poor predictive performance of large-scale ecological mapping models. *Nat. Commun.* 11, 4540. <https://doi.org/10.1038/s41467-020-18321-y>.
- Popescu, S.C., Zhao, K., Neunschwander, A., Lin, C., 2011. Satellite lidar vs. small footprint airborne lidar: comparing the accuracy of aboveground biomass estimates and forest structure metrics at footprint level. *Remote Sens. Environ.* 115, 2786–2797. <https://doi.org/10.1016/j.rse.2011.01.026>. DESDynI VEG-3D special issue.
- Poulter, B., Frank, D., Ciais, P., Myneni, R.B., Andela, N., Bi, J., Broquet, G., Canadell, J.G., Chevallier, F., Liu, Y.Y., Running, S.W., Sitch, S., van der Werf, G.R., 2014. Contribution of semi-arid ecosystems to interannual variability of the global carbon cycle. *Nature* 509, 600–603. <https://doi.org/10.1038/nature13376>.
- Prichard, S.J., Kennedy, M.C., Andreu, A.G., Eagle, P.C., French, N.H., Billmire, M., 2019. Next-generation biomass mapping for regional emissions and carbon inventories: incorporating uncertainty in wildland fuel characterization. *J. Geophys. Res. Biogeosci.* 124, 3699–3716. <https://doi.org/10.1029/2019JG005083>.
- PRISM Climate Group, Oregon State University, 2019. 30-Year Normals [WWW Document]. URL <http://prism.oregonstate.edu/> (accessed 1.28.19).
- Qi, J., Chehbouni, A., Huete, A.R., Kerr, Y.H., Sorooshian, S., 1994. A modified soil adjusted vegetation index. *Remote Sens. Environ.* 48, 119–126. [https://doi.org/10.1016/0034-4257\(94\)90134-1](https://doi.org/10.1016/0034-4257(94)90134-1).
- Qi, W., Saarela, S., Armston, J., Ståhl, G., Dubayah, R., 2019. Forest biomass estimation over three distinct forest types using TanDEM-X InSAR data and simulated GEDI lidar data. *Remote Sens. Environ.* 232, 111283. <https://doi.org/10.1016/j.rse.2019.111283>.
- R Core Team, 2018. R: A Language and Environment for Statistical Computing. R Foundation for Statistical Computing, Vienna, Austria.
- Ratnam, J., Bond, W.J., Fensham, R.J., Hoffmann, W.A., Archibald, S., Lehmann, C.E.R., Anderson, M.T., Higgins, S.I., Sankaran, M., 2011. When is a 'forest' a savanna, and why does it matter? *Glob. Ecol. Biogeogr.* 20, 653–660. <https://doi.org/10.1111/j.1466-8238.2010.00634.x>.
- Rautste, Y., 2005. Multi-temporal JERS SAR data in boreal forest biomass mapping. *Remote Sens. Environ.* 97, 263–275. <https://doi.org/10.1016/j.rse.2005.05.002>.
- Rouse, J.W., 1974. Monitoring Vegetation Systems in the Great Plains with ERTS.
- Roussel, J.-R., (documentation), D.A. (Reviews the, features), F.D.B. (Fixed bugs and improved catalog, segment snags), A.S.M. (Implemented wing 2015 for, track_sensor), B.J.-F. (Contributed to R. for, track_sensor), G.D. (Implemented G. for), 2020. lidR: Airborne LiDAR Data Manipulation and Visualization for Forestry Applications.
- Saarela, S., Holm, S., Healey, S.P., Andersen, H.-E., Petersson, H., Prentius, W., Patterson, P.L., Næsset, E., Gregoire, T.G., Ståhl, G., 2018. Generalized hierarchical model-based estimation for aboveground biomass assessment using GEDI and Landsat data. *Remote Sens.* 10, 1832. <https://doi.org/10.3390/rs10111832>.
- Saatchi, S.S., Harris, N.L., Brown, S., Lefsky, M., Mitchard, E.T.A., Salas, W., Zutta, B.R., Buermann, W., Lewis, S.L., Hagen, S., Petrova, S., White, L., Silman, M., Morel, A., 2011. Benchmark map of forest carbon stocks in tropical regions across three continents. *PNAS* 108, 9899–9904. <https://doi.org/10.1073/pnas.1019576108>.
- Schmitt, M., Zhu, X.X., 2016. Data fusion and remote sensing – an ever-growing relationship. *IEEE Geosci. Remote Sens. Magaz. (GRSM)* 4, 6–23.
- Silva, C.A., Hamamura, C., Valbuena, R., Hancock, S., Cardil, A., Broadbent, E.N., de Almeida, D.R.A., Junior, C.H.L.S., Klauber, C., (Library), B.G. (Is the author of the M-1 L.S.F., Library), K.H. (Is the author of the M-1 L.S.F., Library), J.M. (Is the author of the M-1 L.S.F., Library), C.M. (Is the author of the enhanced M-1 L.S.F., 2020. rGEDI: NASA's Global Ecosystem Dynamics Investigation (GEDI) Data Visualization and Processing.
- Simonson, W.D., Allen, H.D., Coomes, D.A., 2012. Use of an airborne Lidar system to model plant species composition and diversity of Mediterranean oak forests. *Conserv. Biol.* 26, 840–850. <https://doi.org/10.1111/j.1523-1739.2012.01869.x>.
- Singh, K.K., Vogler, J.B., Shoemaker, D.A., Meentemeyer, R.K., 2012. LiDAR-Landsat data fusion for large-area assessment of urban land cover balancing spatial resolution, data volume and mapping accuracy. *ISPRS J. Photogramm. Remote Sens.* 74, 110–121. <https://doi.org/10.1016/j.isprsjprs.2012.09.009>.
- Smith, W.K., Dannenberg, M.P., Yan, D., Herrmann, S., Barnes, M.L., Barron-Gafford, G.A., Biederman, J.A., Ferrenberg, S., Fox, A.M., Hudson, A., Knowles, J.F., MacBean, N., Moore, D.J.P., Nagler, P.L., Reed, S.C., Rutherford, W.A., Scott, R.L., Wang, X., Yang, J., 2019. Remote sensing of dryland ecosystem structure and function: Progress, challenges, and opportunities. *Remote Sens. Environ.* 233, 111401. <https://doi.org/10.1016/j.rse.2019.111401>.
- Sprinkle, W., Klepac, J., 2015. Models of Utah juniper and two-needle pinyon biomass for one site in Southwest Utah. *For. Sci.* 61, 162–168. <https://doi.org/10.5849/forsci.12-541>.
- Storey, J., Choate, M., Lee, K., 2014. Landsat 8 Operational Land Imager on-orbit geometric calibration and performance. *Remote Sens.* 6, 11127–11152. <https://doi.org/10.3390/rs61111127>.
- Taft, J.B., 1997. Savanna and open-woodland communities. In: Schwartz, M.W. (Ed.), Conservation in Highly Fragmented Landscapes. Springer New York, Boston, MA, pp. 24–54. https://doi.org/10.1007/978-1-4757-0656-7_2.
- Tang, H., Armston, J., 2019. Algorithm Theoretical Basis Document (ATBD) for GEDI L2B Footprint Canopy Cover and Vertical Profile Metrics, version 1.0. NASA, Goddard Space Flight Center.
- Vastaranta, M., Yu, X., Luoma, V., Karjalainen, M., Saarinen, N., Wulder, M.A., White, J.C., Persson, H.J., Hollaus, M., Yrttimäki, T., Holopainen, M., Hyppä, J., 2018. Aboveground forest biomass derived using multiple dates of WorldView-2 stereoscopic imagery: quantifying the improvement in estimation accuracy. *Int. J. Remote Sens.* 39, 8766–8783. <https://doi.org/10.1080/01431161.2018.1492176>.
- Vaysse, K., Lagacherie, P., 2017. Using quantile regression forest to estimate uncertainty of digital soil mapping products. *Geoderma* 291, 55–64. <https://doi.org/10.1016/j.geoderma.2016.12.017>.
- Vermote, E., Justice, C., Claverie, M., Franch, B., 2016. Preliminary analysis of the performance of the Landsat 8/OLI land surface reflectance product. *Remote Sens. Environ.* 185, 46–56. <https://doi.org/10.1016/j.rse.2016.04.008>.
- Wallace, A., Nichol, C., Woodhouse, I., 2012. Recovery of forest canopy parameters by inversion of multispectral LiDAR data. *Remote Sens.* 4, 509–531. <https://doi.org/10.3390/rs4020509>.
- Wessels, K.J., Erasmus, B.F.N., Colgan, M., Asner, G.P., Mathieu, R., Twine, W., Van Aardt, J.A.N., Smit, I., 2012. Impacts of communal fuelwood extraction on LiDAR-estimated biomass patterns of savanna woodlands. In: 2012 IEEE International Geoscience and Remote Sensing Symposium. Presented at the 2012 IEEE International Geoscience and Remote Sensing Symposium, pp. 1676–1679. <https://doi.org/10.1109/IGARSS.2012.6351204>.
- Wilson, M.F.J., O'Connell, B., Brown, C., Guinan, J.C., Grehan, A.J., 2007. Multiscale terrain analysis of multibeam bathymetry data for habitat mapping on the continental slope. *Mar. Geod.* 30, 3–35. <https://doi.org/10.1080/01490410701295962>.
- Wu, Z., Dye, D.G., Stoker, J.M., Vogel, J.M., Velasco, M.G., Middleton, B.R., 2016. Evaluating Lidar Point Densities for Effective Estimation of Aboveground Biomass. *International Journal of Advanced Remote Sensing and GIS*.
- Wulder, M.A., Loveland, T.R., Roy, D.P., Crawford, C.J., Masek, J.G., Woodcock, C.E., Allen, R.G., Anderson, M.C., Belward, A.S., Cohen, W.B., Dwyer, J., Erb, A., Gao, F., Griffiths, P., Helder, D., Hermosilla, T., Hippel, J.D., Hostert, P., Hughes, M.J., Huntington, J., Johnson, D.M., Kennedy, R., Kilic, A., Li, Z., Lymburner, L., McCorkel, J., Pahlevan, N., Scambos, T.A., Schaaf, C., Schott, J.R., Sheng, Y., Storey, J., Vermote, E., Vogelmann, J., White, J.C., Wynne, R.H., Zhu, Z., 2019. Current status of Landsat program, science, and applications. *Remote Sens. Environ.* 225, 127–147. <https://doi.org/10.1016/j.rse.2019.02.015>.
- Xu, L., Saatchi, S.S., Shapiro, A., Meyer, V., Ferraz, A., Yang, Y., Bastin, J.-F., Banks, N., Boeckx, P., Verbeeck, H., Lewis, S.L., Muanza, E.T., Bongwele, E., Kayembe, F., Mbenza, D., Kalau, L., Mukendi, F., Ilunga, F., Ebuta, D., 2017. Spatial distribution of

- carbon stored in forests of the Democratic Republic of Congo. *Sci. Rep.* 7, 15030. <https://doi.org/10.1038/s41598-017-15050-z>.
- Yang, J., Weisberg, P.J., Bristow, N.A., 2012. Landsat remote sensing approaches for monitoring long-term tree cover dynamics in semi-arid woodlands: comparison of vegetation indices and spectral mixture analysis. *Remote Sens. Environ.* 119, 62–71. <https://doi.org/10.1016/j.rse.2011.12.004>.
- Zald, H.S.J., Wulder, M.A., White, J.C., Hilker, T., Hermosilla, T., Hobart, G.W., Coops, N.C., 2016. Integrating Landsat pixel composites and change metrics with lidar plots to predictively map forest structure and aboveground biomass in Saskatchewan, Canada. *Remote Sens. Environ.* 176, 188–201. <https://doi.org/10.1016/j.rse.2016.01.015>.
- Zhang, J., 2010. Multi-source remote sensing data fusion: status and trends. *Int. J. Image Data Fusion* 1, 5–24. <https://doi.org/10.1080/19479830903561035>.
- Zhu, Z., Wulder, M.A., Roy, D.P., Woodcock, C.E., Hansen, M.C., Radeloff, V.C., Healey, S.P., Schaaf, C., Hostert, P., Strobl, P., Pekel, J.-F., Lymburner, L., Pahlevan, N., Scambos, T.A., 2019. Benefits of the free and open Landsat data policy. *Remote Sens. Environ.* 224, 382–385. <https://doi.org/10.1016/j.rse.2019.02.016>.
- Zolkos, S.G., Goetz, S.J., Dubayah, R., 2013. A meta-analysis of terrestrial aboveground biomass estimation using lidar remote sensing. *Remote Sens. Environ.* 128, 289–298. <https://doi.org/10.1016/j.rse.2012.10.017>.